# Growth of hexagonal boron nitride from molten nickel solutions: a reactive molecular dynamics study

by

Amin Ahmadisharaf

B.S., Qazvin University, Iran, 2016

---

A REPORT

submitted in partial fulfillment of the
requirements for the degree

MASTER OF SCIENCE

Tim Taylor Department of Chemical Engineering
Carl R. Ice College of Engineering

KANSAS STATE UNIVERSITY
Manhattan, Kansas

2025

Approved by:

Major Professor
Dr. Jeffrey Comer

# Copyright

# Abstract

Metal flux methods are excellent for synthesizing high-quality hexagonal boron nitride (hBN) crystals, but the atomic mechanisms of hBN nucleation and growth in these systems are poorly understood and difficult to probe experimentally. Here, we harness classical reactive molecular dynamics (ReaxFF) to unravel the mechanisms of hBN synthesis from liquid nickel solvent over time scales up to 30 ns. These simulations mimic experimental conditions by including relatively large liquid nickel slabs containing dissolved boron and a molecular nitrogen gas phase. Overall, the reaction takes place almost exclusively on the surface of the liquid nickel, owing to the low solubility of nitrogen in bulk nickel and the intermediate species' preference for the metal–gas interface. The formation of hBN invariably begins by reaction of dinitrogen with nickel-solvated boron atoms at the surface, forming intermediate N–N–B species, which typically evolve into B–N–B units through a short-lived intermediate where a single nitrogen atom is coordinated by one nitrogen and two boron atoms. The resulting B–N–B units, in turn, coalesce with growing hBN nuclei and carry nitrogen between hBN nanocrystals in an Ostwald ripening process. The amount of hBN produced on the tens of nanosecond time scale depends critically on the boron concentration, while having a much weaker dependence on the $N_2$ pressure for the regime considered ($N_2$ pressures of 2.5–10 MPa, Ni-B solutions with 6–12% boron by atom fraction). The highest rate of hBN formation occurs at the lowest temperature considered (1750 K, just above the melting point of nickel), while no hBN sheets are formed at 2000 K or above. An analysis of the transition pathways for nitrogen atoms shows that the final step, incorporation of small B–N motifs into larger hBN sheets, is the rate-limiting step in the regimes considered. While raising the temperature from 1750 to 2000 K has little effect on the formation of intermediates (N–N–B, B–N–B, etc.), the lack of large hBN sheets at temperatures >1900 K

is explained by decreased probability of the final step and increased probability of break-up of hBN into B–N motifs.

# Table of Contents

# List of Figures

# Acknowledgments

I am immensely grateful to Dr. Jeffrey Comer, my advisor, for his guidance and encouragement. His enthusiasm for research has continually inspired me to aspire to new heights and remain steadfast in my academic pursuits.

This work was supported by the U.S. Department of Energy under Grant No. DE-SC0021264-0002. The majority of the computational work in this project was carried out using the Beocat Research Cluster at Kansas State University, which is funded in part by NSF grants CHE-1726332, CNS-1006860, EPS-1006860, and EPS-0919443. I would like to express my sincere gratitude to Dr. James H. Edgar and Dr. Bin Liu for their insightful feedback and valuable comments throughout the course of this project. I am also deeply thankful to Dr. Davood Pourkargar and Prof. Christine Aikens for their support and guidance.

# Dedication

I wish to express my deepest appreciation to my wife, Elena Masrour, for her unwavering support and kindness throughout my studies. She has sacrificed so much to help me achieve this degree, and her belief in our shared success has been invaluable. Dedicated to my parents and family, who have supported me with unwavering love and encouragement despite the distance separating us for many years. Their belief in my potential continues to guide me and has made this achievement possible.

# Preface

While molecular dynamics (MD) simulations offer tremendous opportunities for material science researchers, this research topic opens a way for future studies by making MD simulators more reliable resources for investigating various scientific goals. Moreover, performing these studies entirely through computational means has an important environmental advantage, and that ecological awareness has motivated me to further advance my expertise in computational techniques for applications in materials science and chemical processes. While experiments will often be necessary to test the final predictions of simulations, simulations can point experiments in the right direction, avoiding the associated time, cost, and environmental impact of many trial-and-error experiments.

In particular, boron icosahedral materials stand out for their extraordinary potential in areas ranging from aerospace to human healthcare. These remarkable applications require accurate, fundamental modeling to unlock the full benefits of this versatile material. By pursuing this computational research, I aim to contribute to the broader scientific community by enabling more robust and environmentally responsible investigations into boron icosahedral systems.

# Chapter 1

# Introduction

Hexagonal boron nitride (hBN) has extraordinary potential for applications in electronics,[1;2] catalysis,[3;4] and nanosensors[5] and is among the most promising materials for engineering of single-photon emitters[6], quantum sensors[7–9], and optoelectronics devices.[10–12] Its unique combination of electronic, mechanical, and thermal properties differentiates it from other two-dimensional materials, making it the subject of intense research focus. Synthesis of high quality crystals with few defects or controlled incorporation of functional defects[13] is key to the success of these applications. This drive for purity and quality is rooted in the direct relationship between material defects and device performance, especially in nanoscale applications[14] where even minor imperfections can drastically affect outcomes. A common technique for synthesizing hBN is chemical vapor deposition (CVD)[15] on metal subtrates like copper and platinum[16]. Recent studies on $MoS_2$ synthesis using CVD, such as the work by Arafat et al.,[17] have shown how precursor interactions and reaction intermediates dictate the quality and formation mechanisms of 2D materials. Similar approaches are essential for elucidating the growth pathways of hexagonal boron nitride (hBN) in our study. The growth of monolayer hBN on metal surfaces is primarily governed by surface interactions and diffusion processes, where boron and nitrogen atoms preferentially attach and arrange themselves on specific lattice sites of the metal substrate to form an epitaxial monolayer.[16;18;19] A low-temperature direct synthesis CVD[20] approach has also been developed, enabling the

production of thick multilayered hBN on semiconducting and insulating substrates.

In contrast, flux methods, in which the crystal is grown by precipitation from a molten solvent,[21;22] have the potential to produce higher-quality crystalline hBN at scale, because the reactions occur closer to equilibrium, allowing time for defects to relax. Another advantage of the metal flux methods is that pure elements ($N_2$, $\beta$-B, and doping elements) can be used as sources, rather than molecular precursors (as used in CVD[15;16]) that introduce unwanted or uncontrolled quantities of impurities, particularly hydrogen or carbon. The application of flux methods to hBN synthesis was initiated by Ishii and Sato[23] using molten silicon. Metal fluxes for hBN synthesis have included sodium,[24] nickel,[25] nickel-chromium,[26–30] copper-chromium[31], iron,[32] and iron-chromium.[33] Kubota et al.[26] demonstrated considerable success using Ni-Cr solvent to dissolve boron nitride, subsequently recrystallizing it into large single crystals near 1700–1770 K. Hoffman et al.[27] explored different controlled cooling rates and soak temperatures to optimize hBN synthesis from Ni-Cr solvent, achieving large high-quality single crystals. Further exploring the parameters method, Zhao et al.[29] successfully grew large hBN crystals at 1820 K using a similar Ni-Cr solution. Their work underscores the efficiency of metal flux methods in scaling up the production of hBN crystals while controlling the thermal environment to reduce defects and to enhance the optical properties. Cao et al.[34] found that the size of single crystal hBN could increased by adding carbon to the Ni-Cr flux; however, carbon was also associated with graphene regions throughout the hBN, which were subsequently suppressed by adding Au.

Isotopically enriched elemental sources are typically available at lower cost than similar precursor molecules; hence, the use of elemental sources also facilitates synthesis of isotopically pure hBN. Natural boron consists of two abundant isotopes (19.9% $^{10}$B and 80.1% $^{11}$B), while natural nitrogen is dominated by $^{14}$N (99.6%). Using Ni-Cr flux, Liu et al.[35] produced isoptopically pure hBN with 99% $^{10}$B or 99% $^{11}$B. More recently, Janzen et al.[30] synthesized isotopically pure hBN samples with each of the four combinations of stable boron and nitrogen isotopes, using a two-step method to conserve relatively expensive $^{15}N_2$. They showed distinct phonon scattering and photoluminescence behavior across these four isotopically pure materials as well as hBN with natural isotopic ratios. Hexagonal boron nitride

with natural isotopic abundance has much greater phonon scattering[36;37] than isotopically pure hBN owing to the random distribution of the two prevalent boron isotopes. As a consequence, hBN with 99% $^{10}$B or $^{11}$B exhibits significantly higher thermal conductivity than hBN with natural or equal isotope ratios.[36;38;39] Moreover, there are demonstrated differences in mechanical properties, such the greater elasticity and strength for hBN composed of $^{10}$B and $^{14}$N as compared to other isotopic compositions.[40] This opens the door for precision engineering of hBN properties by isotopic control.

While reaction mechanisms in aqueous or organic solvents can be studied by spectroscopy in the infrared, visible, and ultraviolet ranges, the opacity of metal fluxes precludes easy spectroscopic observation.[41] Molecular dynamics (MD) simulations have been used to study reactions involving boron nitride at the atomic level, revealing many details that would be difficult to observe experimentally. For instance, Krstic et al.[42] employed a quantum–classical method based on density-functional tight-binding (DFTB) to simulate boron nitride cluster formation in the gas phase from diatomic B–N or, more realistically, from borazine precursor. At 2000 K, the diatomic B–N combined to form boron nitride clusters, while, at higher temperatures (4000 and 6000 K), the simulations mostly resulted in $N_2$ gas and solid boron clusters. Reactive molecular dynamics simulations have also been successfully applied to the synthesis of transition metal dichalcogenides (TMDs) on solid substrates, providing atomic-level insights into the reaction mechanisms and growth kinetics of these materials[43–45]. Similarly, larger BN clusters and fewer $N_2$ molecules were formed from borazine at 1500 and 2000 K than at 2500 and 4000 K.

Classical reactive molecular dynamics, as embodied in the ReaxFF framework,[46] typically allows longer time scales and larger systems than quantum methods, but is entirely reliant on the the existence of accurate parameters for the empirical potential energy functions. An early application of the ReaxFF framework was a study of hydrogen storage in BN nanotubes.[47;48] Later Weismiller et al.[49] simulated ammonia borane combustion with ReaxFF, yielding formation of linear BN species; however, their goal was to study to hydrogen release. On the other hand, Lele et al.[50] focused on formation of boron nitride from the gas phase using ReaxFF, with the goal of understanding the role of hydrogen in BN

nanotube synthesis. Perhaps the most realistic simulations yet reported were implemented by Uene et al.[51]. They employed realistic silanol-terminated silicon surfaces and a protocol similar to that used experimentally in atomic layer deposition (ALD), including $BCl_3$ and $NH_3$ precursors and a 4-step pulse and purge cycle ($BCl_3$ pulse, purge, $NH_3$ pulse, purge). Temperatures of >1000 and <1750 K appeared necessary to form boron nitride nanoclusters on the silicon surface. In contrast, disordered films containing large amounts of chlorine and hydrogen were formed at 750 and 1000 K, while at 1750 and 2000 K, few surface structures were formed all. We previously studied the synthesis of hBN on solid Ni surfaces using both density functional theory (DFT) and ReaxFF.[52;53] These calculations showed that the structure of hBN nanoclusters on Ni(111) depends strongly on the B:N ratio, with high B:N ratios (3:1) resulting in relatively disordered hBN clusters, equal proportions (1:1) yielding triangular domains with boron-terminated zigzag edges, and larger nitrogen ratios (1:3) yielding roughly hexagonal clusters with alternating boron and nitrogen-terminated zigzag edges. These studies also highlighted the role of small intermediate BN motifs, including surface-bound BN dimers, linear B–N–B, and $NB_3$ groups.

In this contribution, we employ ReaxFF, supplemented by ab initio MD, to reveal the mechanisms of hBN synthesis from a metal solvent. ReaxFF provides atomic-scale detail and femtosecond time resolution inaccessible to experiment, while also enabling the evolution of thousands of atoms on the nanosecond time scales necessary for spontaneous formation of hBN to be observed. Reaching such time scales for systems of thousands of atoms is difficult or infeasible with quantum methods such as ab initio MD due to their higher computational demands. However, we use ab initio MD to validate the stability and structure of BN motifs appearing the ReaxFF simulations. First, we simulate the components (solid boron or $N_2$ gas) in contact with liquid nickel. Next, we simulate liquid nickel with dissolved boron in the presence of $N_2$ to reveal how these components interact and nucleate hBN growth. The simulations suggest preferential segregation of boron to the liquid Ni surface, which likely accelerates the rate of nucleation at the surface. Furthermore, the simulations reveal various intermediate molecular species are present during hBN nucleation and growth. Following the evolution of these species over time helps us identify the pathways by which nitrogen atoms

from the gas phase become incorporated in hBN sheets. We also study the dependence of the thermodynamics of hBN formation and the rate of hBN growth on the temperature, $N_2$ pressure, and boron concentration. Understanding these the influence of these conditions, as well as roles of intermediate species, may offer guidance for enhancing yield and purity for hBN synthesis from metal solvents.

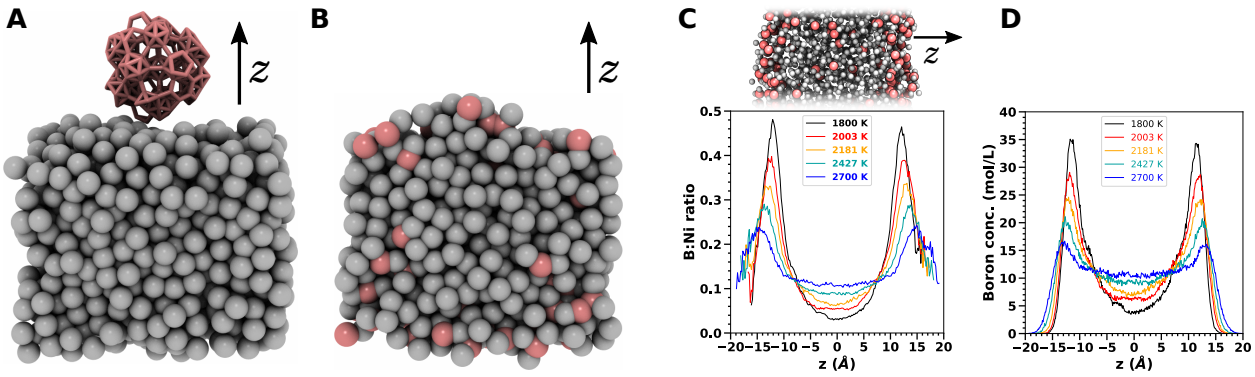


**Figure 1.1**: *Dissolution of boron in liquid nickel and segregation of boron at the liquid nickel surface. (A) Initial simulation structure with a small crystal of β-rhombohedral boron near a liquid nickel surface. Boron and nickel atoms are shown as pink and gray spheres respectively. (B) Structure after 8 ns of simulation at 1900 K showing that the elemental boron crystal dissolves and spontaneously segregates to the nickel surface. Boron-to-nickel ratio (C) or boron concentration (D) along the direction transverse to the liquid nickel slab (the z-axis). Several temperatures are shown, revealing the temperature dependence of boron segregation.*

# Chapter 2

# Methodology

**Reactive molecular dynamics methods.** The reactive molecular dynamics simulations were performed using the ReaxFF framework[46] as implemented in the program LAMMPS[54] with GPU acceleration.[55;56] The ReaxFF parameters for B/N/Ni systems were the same as used in our previous work.[53] These parameters are included in the Supporting Information, as well as in the Zenodo repository for this work (see the section "Data and software availability"). The equations of motion were integrated with a 0.25 fs timestep. For simulations performed at constant volume ($NVT$), the temperature was maintained at the given values using a Langevin thermostat with a 200 ps damping constant. An exception were simulations to calculate diffusion coefficients, which were performed without a thermostat (constant energy, $NVE$). Simulations with constant pressure ($NPT$) are described further below.

**Nickel model.** A face-centered cubic slab of solid nickel was formed by ABC stacking of 12 atom × 12 atom close-packed planes (lattice constant, $a$ =3.524 Å; bond length, $d$ =2.492 Å). Nickel atoms were deleted from the surface to obtain a slab of 1520 atoms. The resulting structure was placed in a periodic system of dimensions 27.89 Å × 32.20 Å × 220.00 Å, which was maintained for subsequent simulations. This nickel slab was continuous in the $xy$ plane, owing to the periodic boundary conditions, while having free Ni(111) surfaces perpendicular to the $z$-axis and a large amount of empty space above and below the slab.

This structure was simulated with the ReaxFF model at 1800 K with fixed volume, forming a liquid slab.

**Temperature replica exchange.** Temperature replica exchange simulations[57–60] were performed with LAMMPS using 20 replicas. Exchanges between replicas were attempted every 1000 steps. The temperatures ranged from 1800 to 2700 K with a constant ratio between consecutive temperatures (rather than a constant increment), which was chosen to give an approximately uniform acceptance rate across the replicas.[61;62] DCD-format files for each temperature ensemble were assembled from the output of LAMMPS using an in-house script (included in the Zenodo repository).

**Model for boron dissolution in nickel.** To study the dissolution of boron in nickel, a quasi-spherical crystal of $\beta$-rhombohedral boron consisting of 208 B atoms was cut from larger $\beta$-rhombohedral structure. This rhombohedral nanocrystal was stable in an isolated form (in the absence of Ni), surviving equilibration where the temperature was raised from 0 to 1900 K over 0.5 ns. During this time, the root-mean-square deviation (RMSD) from the ideal crystal remained below 0.8 Å (after performing a rigid fit to the ideal reference) and 6 full $B_{12}$ icosahedra remained at the end. This equilibrated boron crystal structure was placed near the equilibrated liquid nickel slab and simulated at 1900 K for 13 ns. The boron crystal slowly dissolved into the liquid nickel and no trace of the original crystal remained after 6.7 ns. To obtain the temperature dependence of the boron distribution, the system subsequently underwent temperature replica exchange with 20 replicas with temperatures from 1800 to 2700 K. This resulted in an equilibrated Ni/B system with 1520 Ni atoms and a boron atomic fraction of 12.0% (B:Ni mole ratio of 13.7%), which corresponds to solution that is 2.5% boron by mass. According to the experimentally derived Ni–B phase diagram,[63] this concentration of boron is well below the solubility limit for the temperatures considered in this work.

**Model for $N_2$–nickel interaction.** To study the interaction of $N_2$ with nickel alone, the boron atoms were deleted from the last frame at the base temperature (1800 K). The result was a 27.89 Å × 32.20 Å nickel slab continuous in the $xy$ plane (owing to the periodic boundary conditions), consisting of 1520 Ni atoms. This pure Ni system was equilibrated using temperature replica exchange for 0.3 ns. After extracting the final frame at 1800 K, we randomly placed $N_2$ molecules at a distance >12 Å from the Ni slab. Systems with 60, 120, and 240 $N_2$ molecules were simulated at constant pressures of 84, 168, and 336 atm, respectively; hence, they all maintained sizes of ≈ 200 Å along the $z$ axis. Each of these systems was simulated for 5 ns to observe the interaction of $N_2$ with liquid Ni.

**Model for hBN synthesis.** These simulations began with the equilibrated liquid nickel/boron slab created as described in "Model for boron dissolution in nickel". Simulations of hBN formation were performed by randomly placing 88 $N_2$ molecules at distances > 12 Å from the Ni surface. These simulations were run for 20–30 ns at temperatures of 1750, 1800, 1900, 2000, 2200, and 2700 K, with the size of the system was kept at 27.89 × 32.20 × 220.00 $Å^3$.

**Model for constant pressure simulations.** These simulations began with the equilibrated liquid nickel/boron slab created as described in "Model for boron dissolution in nickel". Boron atoms were deleted at random to produce a system with 104 boron atoms. Simulations of constant pressure were performed by randomly 208 $N_2$ molecules at distances > 8 Å from the Ni surface. These simulations were run for 15 ns at 1750 K and 25, 50, and 100 atm, using the Nosé-Hoover style barostat[64;65] with the equations of motion of Shinoda et al.[66] The barostat was applied to only the $z$-dimension of system, and the size in the $xy$-plane was kept at 27.89 × 32.20 $Å^2$. The simulation systems included large volumes of $N_2$ gas to maintain pressure even as $N_2$ was being depleted at the surface. The initial $z$-dimensions of the system were chosen using the ideal gas law so that the initial pressures were approximately the same as the barostat set points (582, 1165, and 2329 Å for pressures of 100, 50, and 25 atm, respectively). The $z$-axis dimensions of the systems gradually decreased during the simulations due to the consumption of $N_2$; however, the systems maintained large

$z$ dimensions throughout (exceeding 300 Å in all cases).

**Identification of molecular species.** Using an in-house script included in the Zenodo repository, we calculated the number of each common molecular species observed during the simulation (Figure 3.4). These molecular species were identified by finding the N and B neighbors of each N atom at a distance of $< 2.1$ Å. Nitrogen atoms with no N or B neighbors were considered atomic N, which were invariably coordinated by liquid Ni. For the purposes of this analysis, Ni atoms were *not* counted as a neighbors. N atoms with a single N neighbor were labeled $N_2$ nitrogen atoms, if this second atom had no other neighbor. If the second atom had another neighbor, they were labeled N–N–.... Nitrogen atoms having a single B neighbor, were either labeled as free BN nitrogen atoms or as N–B..., if the B atom had additional neighbors. Similarly, N atoms with exactly two neighbors but no next-nearest neighbors were labeled as free NNB or BNB, depending on whether the neighbors were N and B or both B, respectively. When there were next-nearest neighbors, these groups were labeled as ...N–N–B... or ...B–N–B..., respectively. Nitrogen atoms with exclusively 3 boron neighbors, where each of these three B neighbors had another 2 N neighbors were labeled as hBN nitrogen atoms. Nitrogen atoms with 3 B neighbors that did not fulfill this criterion were labeled as $NB_3$ and typically represented small hBN nuclei or edges of larger hBN sheets, as well as free $NB_3$ groups. Nitrogen atoms with three neighbors, including 1 N and 2 B, were labeled as $N_2B_2$.

**Minimal model for comparison with ab initio MD.** The B–N and BNB motifs were extracted from the ReaxFF simulation at 1750 K and placed on top of a $15 \times 16 \times 13$ Å$^3$ slab of liquid nickel. These systems contained 185 nickel atoms and a single B–N or BNB motif and were equilibrated at 1800 K using a Langevin thermostat in a $15 \times 16 \times 60$ Å$^3$ system for 500 ps under ReaxFF. A frame was extracted from the equilibration trajectory for ab initio molecular dynamics at 72.92 ps for the B–N motif and 92.22 ps for the BNB motif. The first 10 ps of the ReaxFF simulations, and the first 0.04 ps of the ab initio simulations were discarded before calculating the statistics and distribution in Figure 3.6.

**Ab Initio molecular dynamics methods.** The ab initio Molecular Dynamics (AIMD) simulations were performed using the Vienna ab initio Simulation Package[67;68]. For general settings, the wave functions of the valence electrons of B, N, and Ni were approximated using the projector augmented wave (PAW) method[69], with the plane-wave basis set energy expanded up to 350 eV. Spin polarization was permitted. The GGA Perdew-Burke-Ernzerhof (PBE) functional was used to account for the electron exchange-correlation effects[70]. The break condition for electronic self-consistent iteration was $1.0 \times 10^{-5}$ eV. Initial structures representing the molten Ni flux interface were extracted from the classical MD, consisting of 185 Ni atoms. One B–N or B–N–B motif unit was included, and their initial configurations on the Ni flux were also determined from the MD based on ReaxFF. The dimensions of simulation box are 15 Å × 16 Å × 50 Å. All AIMD jobs were performed using the canonical ensemble with temperatures fixed at 1800 K, under which hBN growth was observed in this work. The temperature was controlled using the Nosé-Hoover thermostat[64;65]. The time step of 1 fs was used and the trajectory is saved every 5 fs.

**Model for diffusion at the nickel surface.** To study diffusion of boron and nitrogen species at the liquid nickel surface, the Ni slab used for previous simulations was tiled 2 × 2 in the $xy$ plane, yielding a 55.8 Å × 64.4 Å slab with 6080 Ni atoms. All non-nickel atoms were deleted except for 4 surface N atoms, 4 surface B atoms, or 4 free BNB groups, creating three new systems. A fourth system was created by deleting all N and B atoms except for two identical images of a small hBN sheet (25 N and 28 B atoms). For each system, 40 simulations, each of 0.1 ns, were performed without a thermostat (constant energy) beginning from different random velocities chosen from a Maxwell-Boltzmann distribution. Mean squared deviations were calculated by splitting the center-of-mass trajectories for each chemical group into 5 ps subtrajectories.

## Data and software availability

LAMMPS input files, including structure files and configuration files, along with output (LAMMPS log files, LAMMPS restart files, and downsampled DCD-format trajectory files) are freely available for download from Zenodo (https://doi.org/10.5281/zenodo.11037080). We have also included analysis scripts and the processed data produced by these scripts.

# Chapter 3

# Results and Discussion

**Dissolution of boron into liquid Ni.** Experiments have shown that boron is soluble in liquid nickel up to an atomic fraction of 61% for temperatures above the melting point of pure nickel (1728 K).[63] Consistent with this, our simulations at 12% boron (208 B and 1520 Ni atoms) show full dissolution of solid boron into liquid nickel. Figure 1.1A displays the initial structure, where a cluster of $\beta$-rhombohedral boron has been placed near the surface of a 3 nm-thick slab of liquid Ni. After 1.1 ns of simulation at 1900 K, this cluster has fully dissolved into the liquid Ni, as shown in Figure 1.1B. Furthermore, we find a marked tendency of boron to segregate to the surface of the liquid, at least with the ReaxFF parameters used in this work. Figure 1.1C,D quantifies this behavior, by plotting the boron-to-nickel ratio and boron concentration, respectively, along the $z$-axis, revealing the extent of boron segregation to the interface and its dependence on temperature. At 1800 K, the peaks near $z = \pm 10$ Å show a 15-fold greater B:Ni ratio at the surface than in the bulk liquid Ni. As might be expected from entropic considerations, the concentration profiles become more uniform with increasing temperature. The segregation is increasingly less pronounced for higher temperatures, with the surface B:Ni ratio only being about twice that in the bulk at 2700 K. Because of this, our simulations at different temperatures but with equal numbers of boron atoms correspond to different equilibrium bulk boron concentrations, ranging from 3.9 mol/L at 1800 K to 10.5 mol/L at 2700 K. The symmetrical nature of the peaks about

the $z$-axis suggests that the simulations were sufficiently long (1.1 ns of parallel tempering) to equilibrate the boron distribution. The segregation of boron to the surface implies that the amount of boron available for hBN formation at the interface is higher than might be expected from the bulk boron concentration.

**Dissociation of $N_2$ gas in liquid Ni is rare.** We considered two hypothetical pathways for hBN to form from boron solutions in liquid Ni exposed to $N_2$ gas. The first possibility is that the $N_2$ dissociates into atomic N and dissolves into the liquid Ni solution. This dissolved atomic N then later reacts with dissolved boron to form hBN. In the second pathway, nitrogen remains as $N_2$ until making contact with boron, which facilitates its dissociation. To study the first pathway, where $N_2$ dissociates before making contact with boron, we performed a series of simulations of a pure Ni slab in contact with $N_2$ gas at pressures ranging from 8.5 to 33.8 MPa (84 to 334 atm) and temperatures from 1750–2700 K using a 3 nm-thick slab of liquid Ni. Each simulation reached at least 5 ns of simulated time. In none of these simulations did $N_2$ dissociate into atomic nitrogen. Experimental data at 1823 K and the associated Sievert's law constant[71] predict that on average one or fewer dissolved N atoms should be present in our systems (0.53 and 1.06 atoms at 84 and 334 atm, respectively). Therefore, either the rate of N dissociation is too low to be observed in a 5 ns simulation or the process is not represented well by the ReaxFF model. In any case, the small concentration of dissociated N expected from the experiments is insufficient to drive the rapid hBN growth seen in the simulations below. These simulations suggest that the second pathway dominates under the conditions considered, with $N_2$ dissociating only after bonding with boron. The first pathway, whose first step is dissociation of $N_2$ in the absence of boron, appears much slower than the second pathway when boron is plentiful; however, this pathway could still be relevant in systems with very low boron concentrations. Moreover, the addition of chromium, which is commonly used for hBN synthesis from metal fluxes, increases the nitrogen solubility by many times,[71] and could lead to the first pathway becoming dominant.

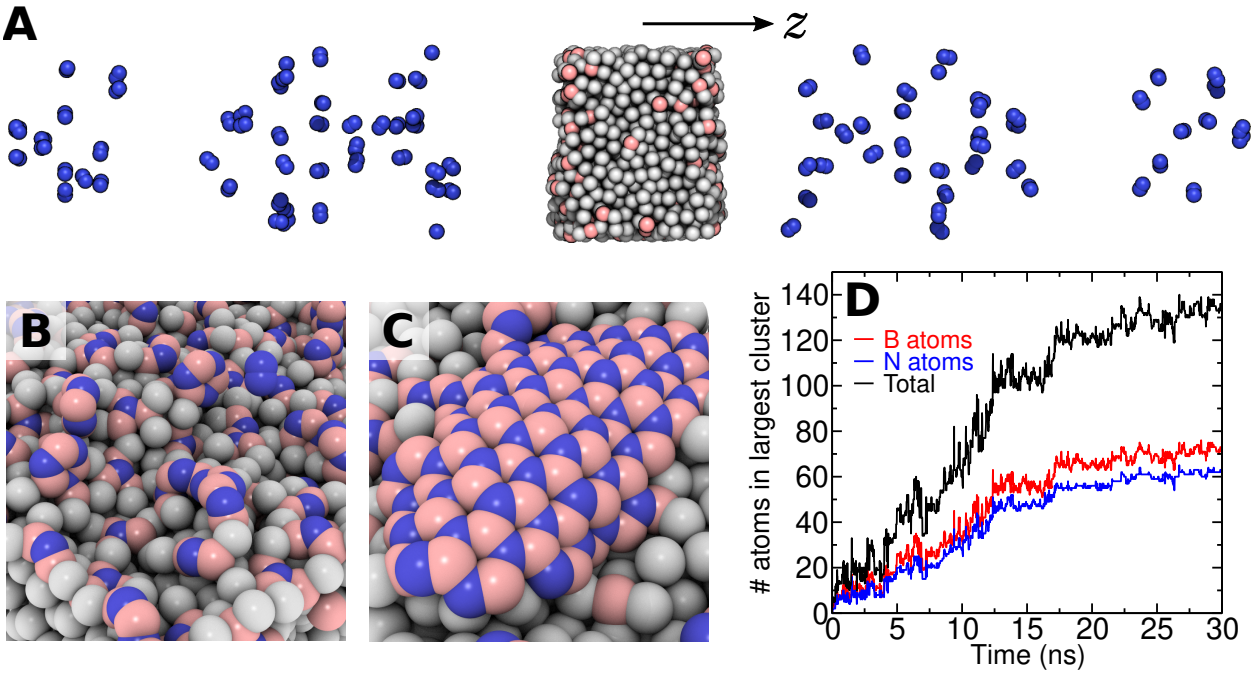


**Figure 3.1**: *Spontaneous formation of hBN at the interface between $N_2$ gas and liquid Ni with dissolved boron. (A) Initial system setup including a liquid Ni slab (equilibrated with dissolved boron) and an $N_2$ gas phase region (B, pink; N, blue; Ni, gray). (B) The same system after 4 ns of simulation at 1750 K, showing transient boron–nitrogen species bound to the interface. (C) A large hBN cluster formed spontaneously on liquid Ni after 27 ns. (D) The size of the largest connected hBN cluster (in number of atoms, counting both B and N) present in the simulation as a function of time. At the end of the simulation (30 ns), each of the two surfaces of the slab is partially covered by one large hBN cluster of >120 atoms*

**Formation of hBN at liquid the Ni–$N_2$ interface.** To emulate hBN synthesis under conditions similar to experiments, we simulated boron solutions in nickel solvent exposed to $N_2$ gas. These simulations were performed at temperatures from 1750 to 2700 K. The size of the simulation system was fixed in these simulations, so that the pressure, initially 123–190 atm, decreased during the simulations as $N_2$ was consumed. Constant pressure simulations, which might be more directly compared to experiment, are described in the next subsection. The simulations were begun from the previously equilibrated liquid Ni slab ($27.9 \times 32.2$ Å$^2$) containing dissolved boron. The initial setup is depicted in Figure 3.1A, showcasing a cross section view of the liquid nickel slab, boron already dissolved in the slab, and $N_2$ randomly distributed in the box. As shown in Figure 3.1B, after 4 ns of simulation at 1750 K, boron–nitrogen species have formed, including B–N–B and hexagonal $B_3N_3$ units. These boron–nitrogen species invariably stay at the Ni surface and do not enter the bulk Ni phase. By 20 ns, large hBN sheets with the expected crystal geometry have formed on both free surfaces of the liquid Ni slab (Figure 3.1C). By the end of the simulation (32.6 ns), two large hBN clusters on each surface cover almost half of the available interfacial area, as shown in Figure S1 of the Supporting Information. The largest covalent boron–nitrogen cluster (Figure S1A), consisting of 141 atoms, dominates the lower surface, while the second largest cluster (Figure S1B), consisting of 125 atoms, occupies much of the upper surface.

The number of atoms in the largest covalent boron–nitrogen cluster is tracked in Figure 3.1D. The increase in the total number of atoms within the cluster indicates active aggregation and growth phases, particularly pronounced until about 13 ns. The growth subsequently slows as the reactant species, such as free boron atoms and $N_2$ molecules, are depleted, as quantified further below. The number of boron atoms in the cluster is always slightly larger than the number of nitrogen atoms, because edges of the hBN sheets are mostly boron-terminated. This is likely dependent on the B:N ratio (here there are 208 B and 176 N atoms in the system).

As noted in the previous subsection, $N_2$ alone did not dissociate on pure liquid Ni on the 5 ns time scale. Hence, the spontaneous growth of hBN within a few nanoseconds in Figure 3.1D demonstrates that hBN formation begins by reaction between molecular $N_2$ and

dissolved boron at the Ni surface.

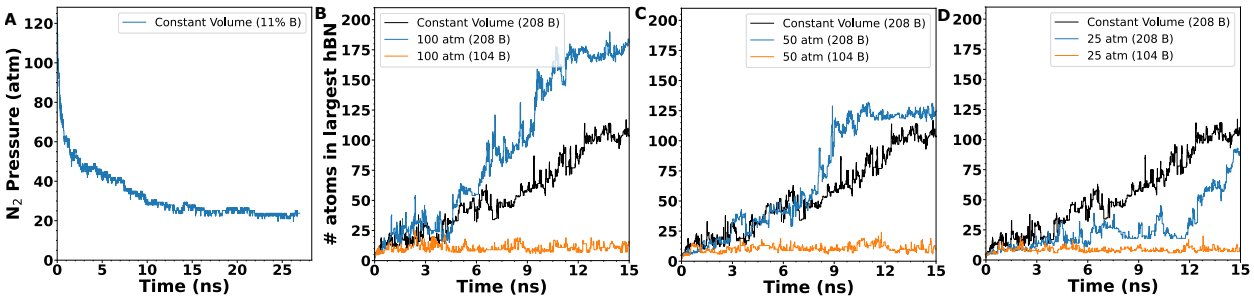


**Figure 3.2**: *Dependence of hBN growth on pressure and boron concentration. (A) $N_2$ pressure during a 30 ns simulation under constant volume conditions, highlighting a sharp initial decline due to reaction of the $N_2$ with boron on the nickel surface. (B–D) Comparison of hBN growth for different $N_2$ pressures and different initial boron concentrations. Plotted is the number of atoms in the largest covalent boron–nitrogen cluster. For reference, the corresponding curve for the constant volume simulation is shown in each panel. $N_2$ pressures shown are 100 atm (B), 50 atm (C), and 25 atm (D). The systems contained 208 or 104 boron atoms and 1520 atoms of liquid nickel. The temperature was 1750 K.*

**Influence of $N_2$ Pressure and Boron Concentration on hBN Growth** The simulation in previous subsection and illustrated in Figure 3.1 was performed at a constant volume and with a constant number of the nitrogen atoms. In this case, the pressure of the $N_2$ in the gas phase diminished during the reaction (Figure 3.2A). However, in typical experiments $N_2$ gas is supplied continuously. Hence, we performed additional simulations at constant pressure with large $N_2$ gas reservoirs to better mimic experimental conditions. We considered three $N_2$ pressures (25, 50, and 100 atm) and, to determine the influence of the boron concentration, two B:Ni ratios (104:1520 and 208:1520). These pressures, while higher than the near atmospheric pressure used in experiments, can still be considered low for the purpose of crystal synthesis ("high pressure" usually implies gigapascals). Moreover, such pressures are unlikely to alter the reaction pathways and enable the reactions to be simulated on time and size scales accessible to ReaxFF.[50;72]

For the systems with 104 boron atoms, almost no hBN is formed irrespective of the $N_2$ pressure, with fewer than 20 atoms in any hBN cluster after 15 ns of simulation (Figure 3.2B–D). Hence, at this concentration, the incorporation of boron appears to be the rate-limiting

step. Going to 208 boron atoms drastically increases hBN growth, with hBN nanosheets of more than 85 atoms forming within 15 ns at all $N_2$ pressures considered. The growth rate and largest cluster size at the end of the simulation depend moderately on the $N_2$ pressure, with a factor of 4 increase in pressure (from 25 to 100 atm) leading to an increase in the largest cluster size by only a factor of 2 (85 versus 175 atoms). The difference in the growth rate between 50 and 100 atm is small, suggesting the rate is controlled by boron availability. The initial growth rate is much slower at 25 atm, suggesting that the $N_2$ pressure becomes a limiting factor in this regime; however, as time progresses, the number of atoms in the largest cluster at 25 atm begins to catch up with the simulations at higher pressure. The time required for this rapid growth would likely vary with different realizations of the simulation. Note that the size of the largest hBN cluster in the constant volume simulation lies between that for pressures of 50 and 25 atm, which is consistent with the average $N_2$ pressure during the constant volume simulation (Figure 3.2A). These results confirm that that boron concentration is a key variable in controlling both the growth rate and the size of the resultant hBN structures.

**Species present during hBN formation.** During the simulations of hBN formation, a number of different intermediate species of varying stability can be identified. Figure 3.3A is a rendering from a simulation at 1750 K showing the various species present at the Ni surface during the formation of hBN. These species include molecular $N_2$, dissociated N atoms bound to the Ni surface, and isolated $Ni_2B$–N–$BNi_2$ motifs, which we will refer to as "free BNB" for simplicity. The image also includes longer linear B–N chains and a roughly triangular hBN nanocrystal.

In Figure 3.3B,C, we quantify the different species by tracking the local environment of each nitrogen atom. These figures depict the number of nitrogen atoms in each category as a function of time, revealing how their concentrations evolve and signifying reaction progress, species stability, and possibly their roles in the formation of hBN. The species appear to be distinguished by N–N, B–N, and B–B bonds, so, for simplicity, bonds to Ni atoms are not considered, and Ni is treated as the background. For instance, N atoms bonded to no

other atoms except Ni are considered atomic nitrogen, while those N atoms bonded to only a single N (again ignoring bonds to Ni) are identified as $N_2$ nitrogen atoms. The number of $N_2$ nitrogen atoms (and likewise the number of $N_2$ molecules) rapidly declines during the simulation, indicating its reaction with boron at the interface. This reaction leads to formation of NNB intermediates, which are individually short-lived, but produced throughout the simulation. The number of NNB intermediates peaks early in the simulation (at 0.36 ns) when the reactants ($N_2$ and surface B) are most plentiful (see inset of Figure 3.3C). These intermediates are transformed into isolated linear BNB ("free BNB") or ...B–N–B..., which we refer to as "linked BNB". Linked BNB refers to nitrogen atoms that are bonded to exactly two B atoms where at least one of these B atoms is bonded to another N or B atom. Nitrogen atoms categorized as "linked BNB" represent edges of hBN sheets or linear B–N chains longer than BNB. The numbers of nitrogen atoms in both the free and linked BNB species rise rapidly, peaking within 5 ns, and then slowly declining over tens of nanoseconds to relatively steady values.

There are also a number of minor intermediates that appear in small amounts during the simulation, including isolated diatomic B–N and atomic N. Atomic N is quite rare, with no more than 4 atoms existing at any one time (Figure 3.3C). The number of nitrogen atoms categorized as "other" is small, implying that the our categorization scheme represents all plentiful species.

Nitrogen atoms bonded to exactly three boron atoms are categorized as hBN/$NB_3$, usually corresponding to hBN sheets or hBN nuclei, but sometimes representing free $NB_3$ groups. The number of hBN/$NB_3$ nitrogen atoms rose during the simulation, indicating growth of the hBN sheets, until reaching a plateau after 20 ns. At this time, the concentration of reactants ($N_2$ and free B) and intermediates has been depleted to the point that a dynamic equilibrium is reached between the hBN sheets and intermediate species: the hBN sheets gain atoms from combination with intermediates, while also breaking down into intermediates at a nearly equal rate.

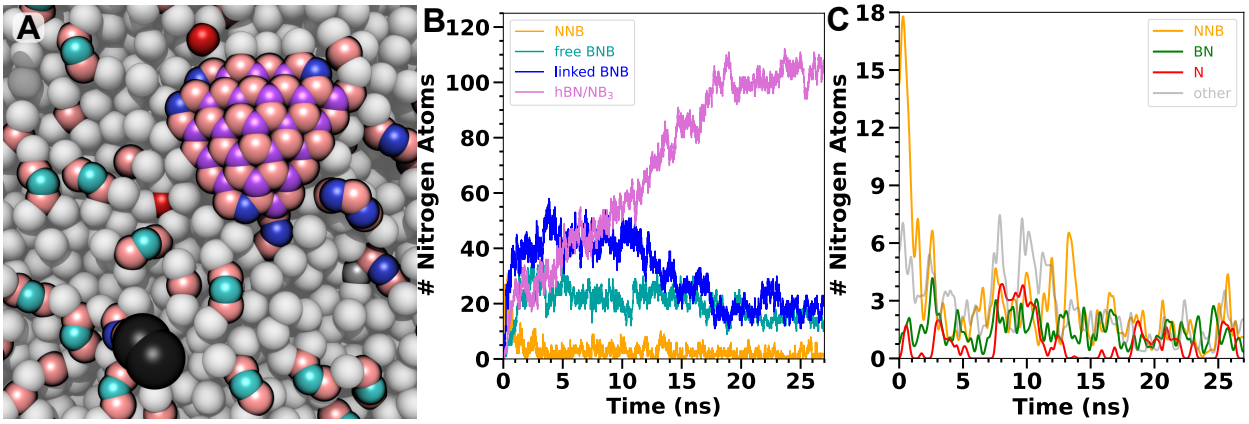


**Figure 3.3**: *Visual and quantitative analysis of boron–nitrogen species during hBN formation. (A) Simulation snapshot illustrating the species appearing during hBN formation, with nitrogen atoms colored according to what species they occur in ($N_2$ gas, black; atomic N, red; free BNB, cyan; linked BNB, blue; $hBN/NB_3$, purple; other, dark gray). Nickel is lighter gray and boron is pink. (B,C) Temporal evolution of nitrogen atom counts for various species during hBN formation. In panel C, a gaussian filter was applied to the raw data with a standard deviation of 0.05 ns for clarity. This simulation was performed at constant volume at 1750 K, beginning with 88 $N_2$ molecules (176 N atoms).*

**Temperature dependence of hBN formation.** At the lowest temperatures (1750, 1800, and 1900 K), the resulting hBN sheets (Figure 3.4A) incorporate most of the boron and nitrogen present in the system. As shown in Figure 3.4B, the rate of formation of hBN sheets, as reflected in the quantity of $hBN/NB_3$ nitrogen atoms, is lower at higher temperatures and appears to saturate with only small boron–nitrogen clusters for $T \geq 2000$ K. Hence, there may exist a critical temperature between 1900 and 2000 K above which formation of relatively large hBN sheets is suppressed.

Despite this lack of hBN sheet formation, the number of various intermediate species increases with temperature. For instance, linked BNB groups (...B–N–B...), which are a necessary intermediate for hBN formation, are created in greater amounts at 2200 K than at temperatures below 1900 K (Figure 3.4B). Also, the amount of free B consumed (binding to N) is similar between 1900 and 2000 K (Figure 3.4D), despite the much reduced quantity of hBN at 2000 K. These results suggest that it may be the final steps of forming large hBN sheets that are relatively disfavored at high temperature, rather than any of the preceding reactions. Despite the fact that $N_2$ is cleaved more easily at higher temperature, forming

more atomic N (Figure 3.4E), there is more $N_2$ at higher temperature (Figure 3.4F) because less nitrogen is bound in hBN. We further investigate the rates of these reactions and how they change with temperature in the following subsections.

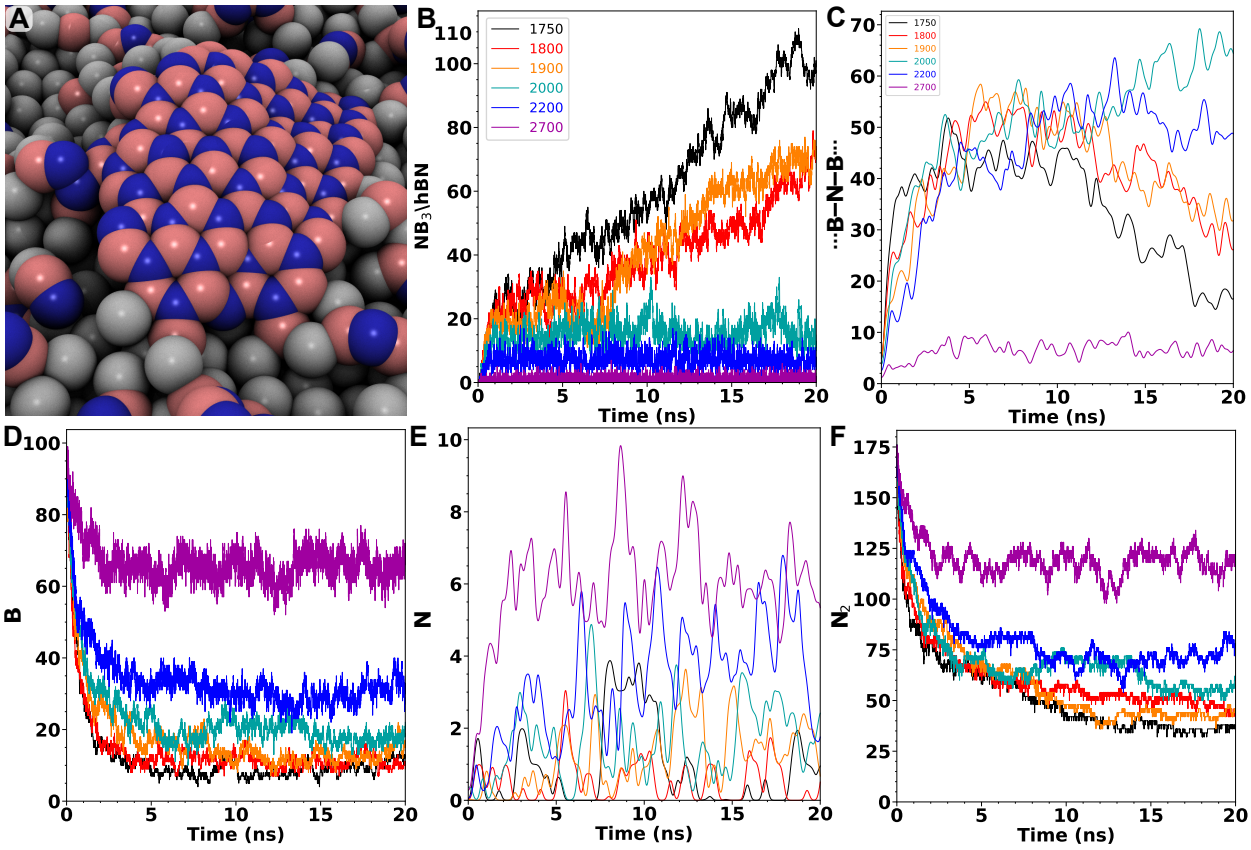


**Figure 3.4**: *Analysis of species present during hBN synthesis at a range of temperatures. (A) hBN sheet formed at 1750 K. (B–F) counts of different species during synthesis at temperatures of 1750, 1800, 1900, 2000, 2200, and 2700 K. Species shown are (B) hBN/$NB_3$ nitrogen atoms, (C) ...B–N–B... nitrogen atoms, (D) free boron atoms, (E) free atomic nitrogen, and (F) $N_2$ nitrogen atoms. Species are defined as in Figure 3.3A. In panels C and E, a gaussian filter was applied to the raw data with a standard deviation of 0.05 ns for clarity.*

**Pathways from $N_2$ to hBN.** The pathways taken by atoms during the synthesis process reveal the chemical mechanisms of hBN synthesis. The changing propensities for these pathways with different synthesis conditions ($N_2$ pressure, boron concentration, and temperature), may be linked with the defect density and morphology of the resulting hBN crystals. For this reason, we analyzed the pathways taken by nitrogen atoms as they go from being

part of the $N_2$ gas phase to form hBN sheets at two different temperatures, 1750 and 2000 K (Figure 3.5). Here, as above, we ignore bonds to Ni and consider only the bond network involving B and N atoms to distinguish the motifs.

Figure 3.5A is an example of the states visited by a single nitrogen atom that begins in the $N_2$ gas phase and progresses through various intermediate surface species before joining a large hBN sheet. First, we see that this nitrogen atom reacts with surface boron at $t =$ 0.28 ns forming an isolated NNB species. From this time until $t = 14.83$ ns, this atom becomes entangled with multiple B and N atoms forming a variety of intermediate motifs, never returning to the $N_2$ gas phase. This atom returns to a linked NNB state after forming linked BNB and then later transiently makes multiple visits to a state where it forms the core of a $B_2N_2$ moiety. During this time, it also forms an isolated $NB_3$ or hBN nucleus multiple times, although these are not incorporated into a larger hBN sheets and do not persist. It also forms free BNB units during several periods. These free BNB units appear as a major intermediate species during the synthesis process (Figure 3.4) and, as detailed further below, are important for transporting N across the surface. Finally, at $t = 13.38$ ns, the $NB_3$ motif becomes incorporated into larger hBN sheet. Apart from a few short transients where atoms in the neighborhood of the selected N atom dissociate from the sheet, the N atom remains part of a large hBN sheet for the remainder of the simulation.

A different nitrogen atom is followed in Figure 3.5B. The progression is much the same as first except that after reaching the $NB_3$ state the first time, it returns to a linked NNB state and then reforms $N_2$, which returns to the gas phase at $t = 4.05$ ns. Later, at $t =$ 15.37 ns, this $N_2$ reacts again with boron on the surface, passing through a series of intermediate states before finally forming part of an hBN sheet at $t = 17.53$ ns. This second example demonstrates the dynamic nature of the synthesis process, which includes backward reactions.

**Statistics of the $N_2$ to hBN pathways.** Figure 3.5A,B provides just two examples. To analyze these transitions statistically, we calculated the transition probabilities for nitrogen atoms to move between each pair of states. This probabilistic analysis is derived from

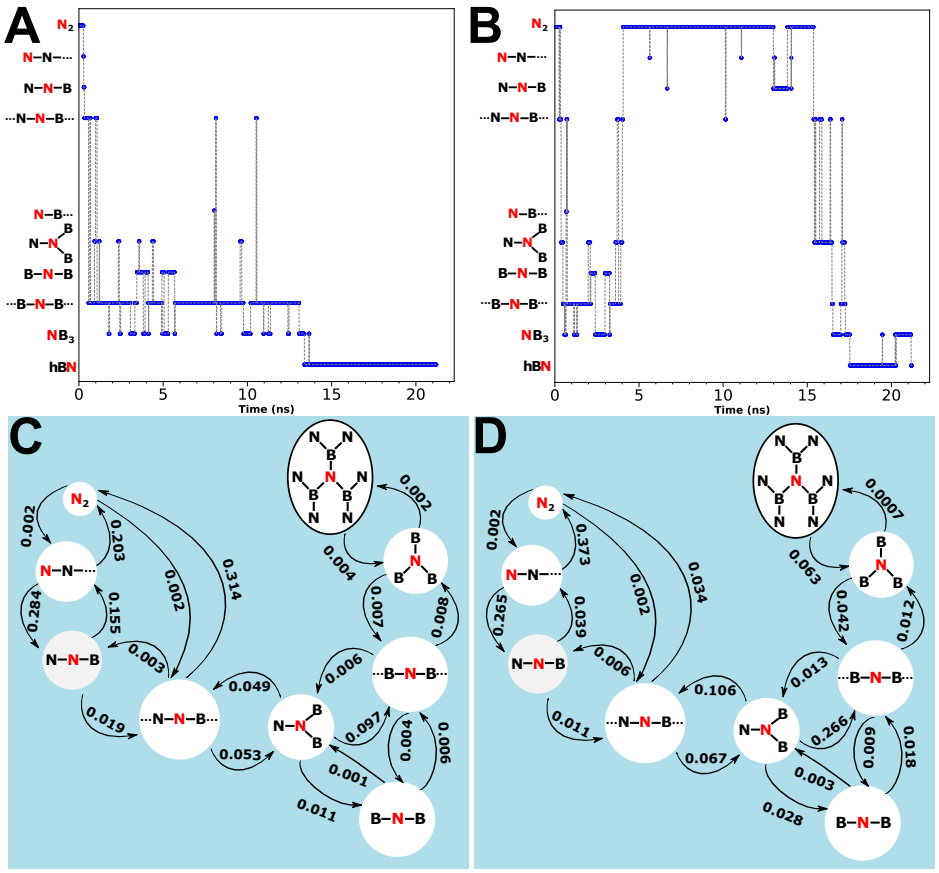


**Figure 3.5**: *Pathways and transition probabilities of atomic nitrogen in hBN synthesis. (A) and (B) illustrate the evolution of single nitrogen atoms during a simulation at 1750 K. (C) and (D) provide a analysis of transition probabilities for nitrogen atoms between different species, highlighting the most likely pathways contributing to hBN lattice formation at 1750 and 2000 K, respectively.*

aggregating individual atom transitions, offering a holistic view of the synthesis dynamics. Note that these transition probabilities depend on the time interval used in the analysis, which here was 2.5 ps. Transition probabilities for the most occupied states at 1750 K are shown in Figure 3.5C. Starting with the transition from molecular nitrogen, $N_2$, we calculate a transition probability of 0.002 to react with boron and form linked NNB (...N–N–B...) structures. This probability is quite low because most $N_2$ remains stably in the gas phase and only reacts when it impinges on the surface; hence, this probability depends strongly on the aspect ratio of the simulation system, as well as the boron concentration at the surface and the temperature. There is a relatively high probability to revert to $N_2$ gas from linked NNB or free NNB (0.15 and 0.31, respectively), underscoring the relative instability of these intermediate species and the stability of the N≡N triple bond. Reaching the $B_2N_2$ state is a critical juncture where the remaining N–N bonds are broken and subsequent intermediate species contain no N–N bonds. $B_2N_2$ exhibits a very low probability for direct reversion to $N_2$ gas (0.00015). For all states beyond this in the diagram, direct reversion to $N_2$ within the analysis interval (2.5 ps) never occurs, which might be expected since these species do not include N–N bonds. After the N–N bonds break, both free BNB and linked BNB chains are the dominant species along the pathway. The probability of transforming from the $B_2N_2$ transition state to the linked BNB (...B–N–B...) state is relativity high (0.097). These linked BNB chains are sometimes small clusters of 4 or 5 non-nickel atoms and, other times, they are edges of larger hBN sheets. Free BNB units also form from $B_2N_2$ with a lower, but still non-negligible probability (0.011); these free BNB units are relatively long-lived since paths away from this state are of relatively low probability.

Here we use "hBN" to denote nitrogen atoms that are bonded exclusively to 3 boron atoms when these boron atoms are also bonded exclusively to two other nitrogen atoms, corresponding to at least a 10-atom nanosheet of hBN. On the other hand, "$NB_3$" denotes nitrogen atoms that do not fulfill the above criteria, but are bonded exclusively to 3 boron atoms, sometimes representing free $NB_3$, but more often representing nitrogen atoms forming small hBN nuclei or near the edges of larger hBN sheets. Transition probabilities from linked BNB to $NB_3$ and from $NB_3$ to larger hBN motifs ("hBN") are quite low at 1750 K, suggesting

that these transformations are likely rate limiting steps for hBN growth.

**Temperature dependence of the $N_2$ to hBN pathways.** Figure 3.5D shows that the pathways at 2000 K are in many respect similar to those at 1750 K; however, there are a few differences that account for the failure to form large hBN sheets at this temperature. First, the transition probabilities from the $N_2$ gas phase are similar, which might be expected since the rate at which $N_2$ strikes the surface only changes little (about 7% greater, $\sqrt{2000\text{ K}/1750\text{ K}} \approx 1.07$). The probability of the reverse transition, from N–N–... to $N_2$, is significantly larger (0.203 at 1750 K and 0.373 at 2000 K), implying that the initial N–N–... motif is less stable at the higher temperature. The transition probabilities from NNB motifs to $N_2B_2$ are comparable for 1750 and 2000 K. On the other hand, transition probabilities from $N_2B_2$ to BNB motifs and from BNB to $NB_3$ motifs are significantly larger at 2000 K. However, the probability of $NB_3$ motifs to incorporate into a larger hBN sheet is about 3 times smaller at 2000 K than at 1750 K. Furthermore, the probability of nitrogen in larger hBN sheets to revert to an incomplete hBN neighborhood ("$NB_3$") is about 16 times larger. Hence, while a higher temperature facilitates some steps in the growth of hBN, the probability of the final step, forming an extended hBN sheet, is significantly reduced at 2000 K compared to 1750 K, and the hBN sheets are much less stable (often breaking up shortly after formation). The structural organization and clustering behavior of boron and nitrogen atoms at 1750 and 2000 K are further elucidated in Supporting Information by radial concentration analyses for B–B and B–N pairs, which highlight key differences in short- and long-range ordering.

**hBN Formation: Surface Interactions and Buoyancy.** It is important to emphasize that the boron–nitrogen species, such as BNB groups, are formed at the liquid Ni surface and remain there throughout our simulations. Atomic N produced during the reaction also remain mostly bound to the interface. On the other hand, Ni-solvated boron atoms are able to transfer between the surface and bulk liquid Ni phase, although the concentration is higher on the surface (Figure 1.1). These results are consistent with our previous calculations with

solid Ni showing that boron easily penetrates sublayers, but that nitrogen remains confined to the surface.[73] Although Ni-solvated nitrogen atoms did enter the bulk liquid Ni on a few occasions, more complex species entering the bulk never occurred. Hence, the synthesis process appears to be confined to the surface and the hBN forms there. However, the inclusion of other components in the solvent (such as Cr) that increase nitrogen solubility may allow more of the reaction to occur in bulk Ni. This surface-confinement mechanism also relates to the potential role of buoyancy in the behavior of hBN. Hexagonal boron nitride has a lower mass density than liquid nickel; hence, once the hBN crystals are large enough, perhaps buoyancy would contribute to keeping them at the interface under typical experimental conditions. However, as detailed below, buoyancy is not relevant for the small sheets formed in our simulations (where gravity is not modeled). To demonstrate this, we find the scale height $H$, given by:

$$H = \frac{k_{\mathrm{B}}T}{(\rho_{\mathrm{Ni}} - \rho_{\mathrm{hBN}})\, V\, g}, \tag{3.1}$$

where $k_{\mathrm{B}}T$ is the thermal energy, $\rho_{\mathrm{Ni}}$ and $\rho_{\mathrm{hBN}}$ are the mass densities of liquid Ni and crystalline hBN, $V$ is the volume of the hBN nanocrystal, and $g$ is the acceleration of gravity. For nanocrystals (volumes less than that of a 10 nm-cube), the scale height is much larger than the size of the apparatus, meaning that the effect of buoyancy is negligible compared to atomic and molecular forces. We hypothesize that hBN is formed at the liquid Ni surface, not due to buoyancy, but because (1) the $N_2$ available there, (2) the concentration of boron is enhanced there, and (3) the nickel–boron species appear trapped there. Therefore, the hBN remains at the interface due to atomic and molecular interactions, with further contributions from buoyancy when the hBN sheets approach the micrometer scale in size. Additionally, the inclusion of other components in the solvent (such as Cr) that increase nitrogen solubility may allow more of the reaction to occur in bulk Ni.

**Validation of predicted species with quantum calculations and experimental data.** Free B–N and BNB motifs are important intermediates in the process of hBN synthesis shown

in Figure 3.5. Therefore, we sought to verify the stability of these motifs on a liquid Ni surface in quantum-level calculations and, where possible, compare to experiment. The B–N and BNB motifs were extracted from the ReaxFF simulation at 1750 K and placed on top of a $15 \times 16 \times 13$ Å$^3$ slab of liquid nickel with free surfaces along the $z$-axis. After equilibration under ReaxFF, these systems were simulated under ab initio molecular dynamics. The DFT-based ab initio simulations verified the stability of the B–N and BNB motifs prevalent in ReaxFF simulations, although the time scales probed by the ab initio method were much shorter (0.24–0.30 ps versus 500 ps).

We also compared the geometry of the motifs between ReaxFF and ab initio calculations. The probability density functions in Figure 3.6A,B compare the B–N bond lengths predicted by ReaxFF to ab initio calculations for B–N and BNB motifs, respectively. While the ReaxFF data show a higher density around the experimental bond lengths for analogous organic compounds, the ab initio data exhibit a broader distribution, suggesting some disagreement between the two methods, particularly for the free BNB motif, though the overall trends remain comparable. Interestingly, ReaxFF and ab initio molecular dynamics exhibit similar peaks in the B–N bond length histogram for the B–N dimer, although the mean value for ab initio MD is somewhat larger. For BNB, the mean value and peak value for ab initio MD is slightly larger than those from ReaxFF.

It is also possible to compare these bond lengths with experimentally derived bond lengths for organic compounds with similar B–N configurations. ReaxFF predicts an average bond length of 1.29 ± 0.15 Å (Mean ± SD) for a free B–N motif on nickel, which lies between that observed experimentally for compounds with B≡N triple bonds, such as *t*Bu–B≡N–*t*Bu (1.26 Å),[74] and B=N double bonds, such as $Mes_2B^-{=}N^+{=}B^-Mes_2$ (1.34 Å)[74] (*t*Bu is the *tert*-butyl group and Mes is the mesityl group, a derivative of 1,3,5-trimethylbenzene). For the BNB motif, the B–N bond lengths predicted by ReaxFF (1.34 ± 0.07 Å, Mean ± SD) are consistent with those in double-bonded B=N=B motifs, such as in $Mes_2B^-{=}N^+{=}B^-Mes_2$ (1.34 Å)[74] and $H_2BNH_2$ (1.39 Å)[75].

It should be noted that the B–N bond lengths in hBN sheets are longer than in these small motifs: 1.45 Å[76;77]. Organic compounds with B–N double and triple bonds appear more

analogous to the B–N and BNB motifs on molten nickel than hBN. The organic compounds are consistent with the coordination observed in the simulation because both the boron and nitrogen atoms in the B–N motif are typically coordinated with one Ni atom each (Figure 3.6A), and the two boron atoms of the BNB motif are coordinated to two Ni atoms each. The B–N motif, therefore, might be more precisely described as $Ni–B^- \equiv N^+–Ni$. Likewise, the BNB motif might be more accurately called $Ni_2B^-{=}N^+{=}B^-Ni_2$.

The BNB angles predicted by the ReaxFF simulations fall within the range observed in the ab initio simulations (Figure 3.6C). However, the ab initio angle distribution is significantly broader, and the mean is significantly smaller (ab initio: 109.3 ° ± 11.61°, ReaxFF: 123.7° ± 6.6°, Mean ± SD). This discrepancy suggests some imperfection in the ReaxFF model; nonetheless, it appears that the stability and structure of Ni-bound BNB motifs predicted by ReaxFF are qualitatively correct.

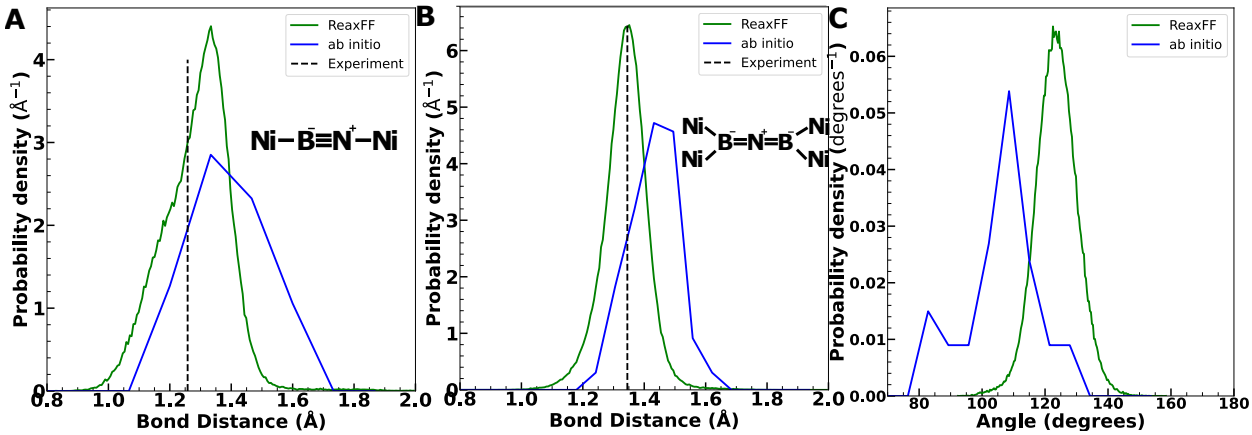


**Figure 3.6**: *Comparison of B–N motif geometry between ReaxFF and ab initio simulations, with additional comparison to experimental values for analogous organic compounds. (A) and (B): Probability density functions of B–N bond distances for free B–N and BNB motifs, respectively, on molten nickel. (C) Probability density function of the B–N–B bond angle in free BNB motifs. The ReaxFF and ab initio data are compared, with experimental values marked by dashed lines, demonstrating a reasonable agreement between the methods.*

**Diffusion of B and N species at the Ni surface.** To understand how boron and nitrogen are transported across the liquid Ni surface, we calculated the two-dimensional diffusion coefficients for different boron and nitrogen species at the liquid nickel surface at 1800 K (Figure 3.7). These species included atomic boron (Figure 3.7A), atomic nitrogen (Figure 3.7B), free BNB groups (Figure 3.7C), and an hBN sheet with a diameter of about 13 Å (Figure 3.7D). Interestingly, free BNB diffuses more rapidly than atomic nitrogen and boron (Figure 3.7E). A least squares fit of the mean square displacements in Figure 3.7 (discarding transient in the 1.6 ps), yields 2D diffusion coefficients of 353, 303, 324, and 88 $Å^2$/ns for atomic B, atomic N, free BNB, and hBN sheet motifs.

Note that "atomic" boron and nitrogen are not really free atoms, but are coordinated with multiple nickel atoms at all times, forming transient compounds like $Ni_3N$ or $Ni_3B$. Compared to boron, nitrogen forms stronger, more directional bonds, reducing its mobility[78]. This explains why boron shows higher mean square displacement values compared to nitrogen. Moreover, both boron and nitrogen exhibit a strong affinity for the interface, and we did not observe them leaving it during our simulations. Hence, because free BNB diffuses rapidly and, as shown in the previous sections, is among the most common intermediate species containing nitrogen, it plays an important role of transporting nitrogen across the surface and exchanging nitrogen between different hBN crystal nuclei. The 13 Å hBN sheet (25 N atoms and 28 B atoms) diffuses much more slowly than the smaller units, such as atomic B and BNB. Hence, growth of hBN appears to be an Ostwald ripening process, wherein larger hBN sheets grow and smaller hBN sheets dissipate mainly by exchanging BNB groups.

# Conclusion

Our study has elucidated the atomic-scale mechanisms underlying synthesis of hexagonal boron nitride (hBN) using nickel metal flux. By leveraging classical reactive molecular dynamics simulations, we have demonstrated the significance of surface phenomena in the formation of hBN. Our simulations reveal that hBN synthesis is initiated by the interaction between $N_2$ and nickel-solvated boron atoms, leading to the formation of NNB intermediate

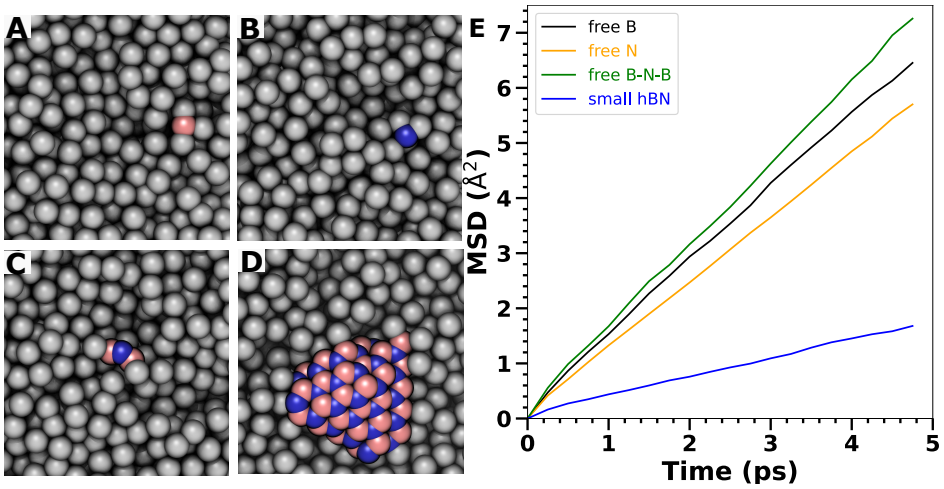


**Figure 3.7**: *Rates of diffusion for boron and nitrogen species at the surface of liquid Ni. (A–D) Images of the considered species at the surface of liquid Ni, including (A) atomic boron, (B) atomic nitrogen, (C) a free BNB group, and (D) a small hBN sheet. (E) Mean square displacement (MSD) in the xy-plane for these species as a function of time, averaged over 5 ps subtrajectories extracted from 40 independent simulations.*

species. These species typically pass through an N-centered $N_2B_2$ transition state to reach relatively stable BNB species. These BNB species then either combine to form hBN crystal nuclei or incorporate themselves into larger hBN sheets. This process is predominantly surface-confined, since these intermediate species appear to exist only at the surface. Calculation of the diffusivity of these intermediate species suggests that the hBN sheets grow by an Ostwald ripening process, with larger sheets tending to accumulate more BNB units, while smaller sheets on average lose nitrogen to break-up into BNB units. Additionally, our research provides insights into the temperature-dependent behavior of hBN formation, revealing a decrease in the rate of hBN sheet formation with increasing temperature from 1750–1900 K and a precipitous drop in hBN formation at 2000 K and beyond. While NNB and BNB intermediates are formed in similar amounts for all temperatures 1750–2200 K, at 2000 K and above the probability of coalescence of $NB_3$ species into larger hBN sheets is much reduced and the probability of break-up of hBN and $NB_3$ into linked and free BNB species is increased. These results suggest that a flux with a lower melting temperature may be desirable, although it remains to seen how the mechanisms of synthesis may change with the composition of the flux. Future studies are needed to determine how the synthesis mech-

anisms might differ with different metal solvents, synthesis conditions, or in the presence of impurities.

# Bibliography


[1] Cory R Dean, Andrea F Young, Inanc Meric, Chris Lee, Lei Wang, Sebastian Sorgenfrei, Kenji Watanabe, Takashi Taniguchi, Phillip Kim, Kenneth L Shepard, and J Hone. Boron nitride substrates for high-quality graphene electronics. *Nature Nanotech.*, 5(10): 722–726, 2010.

[2] Yury Yu Illarionov, Theresia Knobloch, Markus Jech, Mario Lanza, Deji Akinwande, Mikhail I Vexler, Thomas Mueller, Max C Lemme, Gianluca Fiori, Frank Schwierz, and Tibor Grasser. Insulators for 2D nanoelectronics: the gap to bridge. *Nature Comm.*, 11 (1):3385, 2020.

[3] JT Grant, Carlos A Carrero, Florian Goeltl, Juan Venegas, Philipp Mueller, Samuel P Burt, SE Specht, WP McDermott, Alessandro Chieregato, and Ive Hermans. Selective oxidative dehydrogenation of propane to propene using boron nitride catalysts. *Science*, 354(6319):1570–1573, 2016.

[4] Hao Chen, De-en Jiang, Zhenzhen Yang, and Sheng Dai. Engineering nanostructured interfaces of hexagonal boron nitride-based materials for enhanced catalysis. *Acc. Chem. Res.*, pages 10688–10693, 2022.

[5] Andreas Gottscholl, Matthias Diez, Victor Soltamov, Christian Kasper, Dominik Krauße, Andreas Sperlich, Mehran Kianinia, Carlo Bradac, Igor Aharonovich, and Vladimir Dyakonov. Spin defects in hBN as promising temperature, pressure and magnetic field quantum sensors. *Nature Comm.*, 12(1):4480, 2021.

[6] A Sajid, Michael J Ford, and Jeffrey R Reimers. Single-photon emitters in hexagonal boron nitride: a review of progress. *Rep. Progr. Phys.*, 83(4):044501, 2020.

[7] Hongbing Cai, Shihao Ru, Zhengzhi Jiang, John Jun Hong Eng, Ruihua He, Fu-li Li, Yansong Miao, Jesús Zúñiga-Pérez, and Weibo Gao. Spin defects in hBN assisted by metallic nanotrenches for quantum sensing. *Nano Lett.*, 23(11):4991–4996, 2023.

[8] Andreas Gottscholl, Matthias Diez, Victor Soltamov, Christian Kasper, Dominik Krauße, Andreas Sperlich, Mehran Kianinia, Carlo Bradac, Igor Aharonovich, and Vladimir Dyakonov. Spin defects in hBN as promising temperature, pressure and magnetic field quantum sensors. *Nature Comm.*, 12(1):4480, 2021.

[9] Islay O Robertson, Sam C Scholten, Priya Singh, Alexander J Healey, Fernando Meneses, Philipp Reineck, Hiroshi Abe, Takeshi Ohshima, Mehran Kianinia, Igor Aharonovich, and Tetienne Jean-Philippe. Detection of paramagnetic spins with an ultrathin van der Waals quantum sensor. *ACS Nano*, 17(14):13408–13417, 2023.

[10] Jaewoo Shim, Hyung-Youl Park, Dong-Ho Kang, Jin-Ok Kim, Seo-Hyeon Jo, Yongkook Park, and Jin-Hong Park. Electronic and optoelectronic devices based on two-dimensional materials: From fabrication to application. *Adv. Electron. Mater.*, 3(4): 1600364, 2017.

[11] Joshua D Caldwell, Igor Aharonovich, Guillaume Cassabois, James H Edgar, Bernard Gil, and DN Basov. Photonics with hexagonal boron nitride. *Nat. Rev. Mol. Cell Biol.*, 4(8):552–567, 2019.

[12] Biying Tan, You Wu, Feng Gao, Huihui Yang, Yunxia Hu, Huiming Shang, Xin Zhang, Jia Zhang, Zhonghua Li, YongQing Fu, Jia Dechang, Zhou Yu, Xiao Haiying, and Hu PingAn. Engineering the optoelectronic properties of 2D hexagonal boron nitride monolayer films by sulfur substitutional doping. *ACS Appl. Mater. Interfaces*, 14(14): 16453–16461, 2022.

[13] Hongwei Liu, Noah Mendelson, Irfan H Abidi, Shaobo Li, Zhenjing Liu, Yuting Cai, Kenan Zhang, Jiawen You, Mohsen Tamtaji, Hoilun Wong, Yao Ding, Guojie Chen, Igor Aharonovich, and Zhengtang Luo. Rational control on quantum emitter formation

in carbon-doped monolayer hexagonal boron nitride. *ACS Appl. Mater. Interfaces*, 14 (2):3189–3198, 2022.

[14] Wonbong Choi, Nitin Choudhary, Gang Hee Han, Juhong Park, Deji Akinwande, and Young Hee Lee. Recent development of two-dimensional transition metal dichalcogenides and their applications. *Materials Today*, 20(3):116–130, 2017.

[15] Yumeng Shi, Christoph Hamsen, Xiaoting Jia, Ki Kang Kim, Alfonso Reina, Mario Hofmann, Allen Long Hsu, Kai Zhang, Henan Li, Zhen-Yu Juang, et al. Synthesis of few-layer hexagonal boron nitride thin film by chemical vapor deposition. *Nano letters*, 10(10):4134–4139, 2010.

[16] Ki Kang Kim, Allen Hsu, Xiaoting Jia, Soo Min Kim, Yumeng Shi, Mildred Dresselhaus, Tomas Palacios, and Jing Kong. Synthesis and characterization of hexagonal boron nitride film as a dielectric layer for graphene devices. *ACS Nano*, 6(10):8583–8590, 2012.

[17] Abdullah Arafat, Md Sherajul Islam, Naim Ferdous, ASM Jannatul Islam, Md Mosarof Hossain Sarkar, Catherine Stampfl, and Jeongwon Park. Atomistic reaction mechanism of CVD grown MoS2 through moo3 and h2s precursors. *Scientific Reports*, 12(1):16085, 2022.

[18] Hongxia Zhu, Xiaolei Zhao, Huanhuan Li, and Ruiqi Zhao. Revealing stable geometries and magic clusters of hexagonal boron nitride in the nucleation of chemical vapor deposition growth on Ni(111)/Cu(111) surfaces: a theoretical study. *Phys. Chem. Chem. Phys.*, 22(7):4023–4031, 2020.

[19] Md Sherajul Islam, Abdullah Al Mamun Mazumder, Minhaz Uddin Sohag, Md Mosarof Hossain Sarkar, Catherine Stampfl, and Jeongwon Park. Growth mechanisms of monolayer hexagonal boron nitride (h-BN) on metal surfaces: Theoretical perspectives. *Nanoscale Adv.*, 5(16):4041–4064, 2023.

[20] Masaya Yamamoto, Hiromasa Murata, Noriyuki Miyata, Hiroshi Takashima, Masayoshi Nagao, Hidenori Mimura, Yoichiro Neo, and Katsuhisa Murakami. Low-temperature direct synthesis of multilayered h-BN without catalysts by inductively coupled plasma-enhanced chemical vapor deposition. *ACS Omega*, 8(6):5497–5505, 2023.

[21] Jian Wang, Philip Yox, and Kirill Kovnir. Flux growth of phosphide and arsenide crystals. *Front. Chem.*, 8:186, 2020.

[22] Mercouri G Kanatzidis, Rainer Pöttgen, and Wolfgang Jeitschko. The metal flux: a preparative tool for the exploration of intermetallic compounds. *Angew. Chem. Int. Ed.*, 44(43):6996–7023, 2005.

[23] T Ishii and T Sato. Growth of single crystals of hexagonal boron nitride. *J. Cryst. Growth*, 61(3):689–690, 1983.

[24] Masaichi Yano Khin Yap, Mitsuo Okamoto Mitsuo Okamoto, Mamoru Onda Mamoru Onda, Masashi Yoshimura Masashi Yoshimura, Yusuke Mori Yusuke Mori, and Takatomo Sasaki Takatomo Sasaki. Na: a new flux for growing hexagonal boron nitride crystals at low temperature. *Jpn. J. Appl. Phys.*, 39(4A):L300, 2000.

[25] Yoichi Kubota, Kenji Watanabe, Osamu Tsuda, and Takashi Taniguchi. Deep ultraviolet light-emitting hexagonal boron nitride synthesized at atmospheric pressure. *Science*, 317 (5840):932–934, 2007.

[26] Yoichi Kubota, Kenji Watanabe, Osamu Tsuda, and Takashi Taniguchi. Hexagonal boron nitride single crystal growth at atmospheric pressure using Ni-Cr solvent. *Chem. Mater.*, 20(5):1661–1663, 2008.

[27] Timothy B Hoffman, B Clubine, Y Zhang, K Snow, and James H Edgar. Optimization of Ni–Cr flux growth for hexagonal boron nitride single crystals. *J. Cryst. Growth*, 393: 114–118, 2014.

[28] James H Edgar, Timothy B Hoffman, Ben Clubine, M Currie, XZ Du, JY Lin, and

HX Jiang. Characterization of bulk hexagonal boron nitride single crystals grown by the metal flux technique. *J. Cryst. Growth*, 403:110–113, 2014.

[29] Jianguo Zhao, Haichao Wang, Yue Yu, Minhui Yang, Ru Xu, Hui Zhang, Jiangyong Pan, Yuanyuan Li, Xiang Liu, Tao Tao, Zhe d Zhuang, Bin b Liu, and Jianhua Chang. Rapid growth of a 24 $mm^2$ scale hexagonal boron nitride crystal in Ni–Cr solution. *J. Mater. Chem. C*, 11(35):11851–11856, 2023.

[30] Eli Janzen, Hannah Schutte, Juliette Plo, Adrien Rousseau, Thierry Michel, Wilfried Desrat, Pierre Valvin, Vincent Jacques, Guillaume Cassabois, Bernard Gil, and James H. Edgar. Boron and nitrogen isotope effects on hexagonal boron nitride properties. *Adv. Mater.*, 36(2):2306033, 2024.

[31] Naifu Zhang, Naiji Yang, Wenjun Wang, Xin Zhong, and Xiaolong Chen. Growth of hexagonal boron nitride crystals at atmospheric pressure from Cu–Cr flux. *J. Cryst. Growth*, 562:126074, 2021.

[32] Jiahan Li, Junyong Wang, Xiaotian Zhang, Christine Elias, Gaihua Ye, Dylan Evans, Goki Eda, Joan M Redwing, Guillaume Cassabois, Bernard Gil, Pierre Valvin, Rui He, Bin Liu, and James H Edgar. Hexagonal boron nitride crystal growth from iron, a single component flux. *ACS Nano*, 15(4):7032–7039, 2021.

[33] Song Liu, Rui He, Zhipeng Ye, Xiaozhang Du, Jingyu Lin, Hongxing Jiang, Bin Liu, and James H Edgar. Large-scale growth of high-quality hexagonal boron nitride crystals at atmospheric pressure from an fe–cr flux. *Cryst. Growth Des.*, 17(9):4932–4935, 2017.

[34] Jiehua Cao, Ming Tian, Siyuan Zhang, Weiguo Hu, Neng Wan, and Tao Lin. Carbon-related defect control of bulk hBN single crystals growth by atmospheric-pressure metal-flux-based fusion synthesis. *J. Mater. Sci.*, 57(31):14668–14680, 2022.

[35] Song Liu, Rui He, Lianjie Xue, Jiahan Li, Bin Liu, and James H Edgar. Single crystal growth of millimeter-sized monoisotopic hexagonal boron nitride. *Chem. Mater.*, 30 (18):6222–6225, 2018.

[36] L Lindsay and DA Broido. Enhanced thermal conductivity and isotope effect in single-layer hexagonal boron nitride. *Phys. Rev. B*, 84(15):155421, 2011.

[37] Ramon Cuscó, James H Edgar, Song Liu, Jiahan Li, and Luis Artús. Isotopic disorder: the prevailing mechanism in limiting the phonon lifetime in hexagonal BN. *Phys. Rev. Lett.*, 124(16):167402, 2020.

[38] Chao Yuan, Jiahan Li, Lucas Lindsay, David Cherns, James W Pomeroy, Song Liu, James H Edgar, and Martin Kuball. Modulating the thermal conductivity in hexagonal boron nitride via controlled boron isotope concentration. *Commun. Phys.*, 2(1):43, 2019.

[39] Qiran Cai, Declan Scullion, Wei Gan, Alexey Falin, Pavel Cizek, Song Liu, James H Edgar, Rong Liu, Bruce CC Cowie, Elton JG Santos, and Lu Hua Li. Outstanding thermal conductivity of single atomic layer isotope-modified boron nitride. *Phys. Rev. Lett.*, 125(8):085902, 2020.

[40] Alexey Falin, Haifeng Lv, Eli Janzen, James H Edgar, Rui Zhang, Dong Qian, Hwo-Shuenn Sheu, Qiran Cai, Wei Gan, Xiaojun Wu, Elton J. G. Santos, and Lu Hua Li. Anomalous isotope effect on mechanical properties of single atomic layer boron nitride. *Nature Comm.*, 14(1):5331, 2023.

[41] Kourosh Kalantar-Zadeh, Md Arifur Rahim, and Jianbo Tang. Low melting temperature liquid metals and their impacts on physical chemistry. *Acc. Mater. Res.*, 2(8):577–580, 2021.

[42] Predrag S Krstic, Longtao Han, Stephan Irle, and Hiromi Nakai. Simulations of the synthesis of boron-nitride nanostructures in a hot, high pressure gas volume. *Chem. Sci.*, 9(15):3803–3819, 2018.

[43] Shiddartha Paul, Riccardo Torsi, Joshua A Robinson, and Kasra Momeni. Effect of the substrate on MoS2 monolayer morphology: an integrated computational and experimental study. *ACS Applied Materials & Interfaces*, 14(16):18835–18844, 2022.

[44] Yuan Xuan, Abhishek Jain, Suhaib Zafar, Roghayyeh Lotfi, Nadire Nayir, Yuanxi Wang, Tanushree H Choudhury, Samuel Wright, John Feraca, Leonard Rosenbaum, et al. Multi-scale modeling of gas-phase reactions in metal-organic chemical vapor deposition growth of wse2. *Journal of Crystal Growth*, 527:125247, 2019.

[45] Kasra Momeni, Nuruzzaman Sakib, Daniel E Cintron Figueroa, Shiddartha Paul, Cindy Y Chen, Yu-Chuan Lin, and Joshua A Robinson. Combined experimental and computational insight into the role of substrate in the synthesis of two-dimensional wse2. *ACS Applied Materials & Interfaces*, 16(5):6644–6652, 2024.

[46] Thomas P Senftle, Sungwook Hong, Md Mahbubul Islam, Sudhir B Kylasa, Yuanxia Zheng, Yun Kyung Shin, Chad Junkermeier, Roman Engel-Herbert, Michael J Janik, Hasan Metin Aktulga, Toon Verstraelen, Ananth Grama, and Adri CT van Duin. The ReaxFF reactive force-field: Development, applications and future directions. *npj Comput. Mater.*, 2:15011, 2016.

[47] Sang Soo Han, Jeung Ku Kang, Hyuck Mo Lee, Adri CT Van Duin, and William A Goddard. The theoretical study on interaction of hydrogen with single-walled boron nitride nanotubes. I. the reactive force field ReaxFFHBN development. *J. Chem. Phys.*, 123(114703), 2005.

[48] Sang Soo Han, Jeung Ku Kang, Hyuck Mo Lee, Adri CT Van Duin, and William A Goddard. Theoretical study on interaction of hydrogen with single-walled boron nitride nanotubes. II. collision, storage, and adsorption. *J. Chem. Phys.*, 123(114704), 2005.

[49] Michael R Weismiller, Adri CT Van Duin, Jongguen Lee, and Richard A Yetter. ReaxFF reactive force field development and applications for molecular dynamics simulations of ammonia borane dehydrogenation and combustion. *J. Phys. Chem. A*, 114(17):5485–5492, 2010.

[50] Aditya Lele, Predrag Krstic, and Adri CT Van Duin. ReaxFF force field development for gas-phase hBN nanostructure synthesis. *J. Phys. Chem. A*, 126(4):568–582, 2022.

[51] Naoya Uene, Takuya Mabuchi, Masaru Zaitsu, Shigeo Yasuhara, Adri CT van Duin, and Takashi Tokumasu. Reactive force field molecular dynamics studies of the initial growth of boron nitride using BCl3 and NH3 by atomic layer deposition. *J. Phys. Chem. C*, 128(3):1075–1086, 2024.

[52] Song Liu, Adri CT Van Duin, Diana M Van Duin, Bin Liu, and James H Edgar. Atomistic insights into nucleation and formation of hexagonal boron nitride on nickel from first-principles-based reactive molecular dynamics simulations. *ACS Nano*, 11(4): 3585–3596, 2017.

[53] Song Liu, Jeffrey Comer, Adri C. T. van Duin, Diana M. van Duin, Bin Liu, and James H. Edgar. Predicting the preferred morphology of hexagonal boron nitride domain structure on nickel from ReaxFF-based molecular dynamics simulations. *Nanoscale*, 11: 5607–5616, 2019. doi: 10.1039/C8NR10291K.

[54] Steve Plimpton. Fast parallel algorithms for short-range molecular dynamics. *J. Comp. Phys.*, 117(1):1–19, 1995.

[55] H. M. Aktulga, J. C. Fogarty, S. A. Pandit, and A. Y. Grama. Parallel reactive molecular dynamics: Numerical methods and algorithmic techniques. *Parallel Comput.*, 38:245–259, 2012.

[56] H. Carter Edwards, Christian R. Trott, and Daniel Sunderland. Kokkos: Enabling manycore performance portability through polymorphic memory access patterns. *J. Parallel Distr. Comp.*, 74(12):3202 – 3216, 2014. ISSN 0743-7315. doi: https://doi.org/10.1016/j.jpdc.2014.07.003. URL http://www.sciencedirect.com/science/article/pii/S0743731514001257. Domain-Specific Languages and High-Level Frameworks for High-Performance Computing.

[57] Tsuneyasu Okabe, Masaaki Kawata, Yuko Okamoto, and Masuhiro Mikami. Replica-exchange monte carlo method for the isobaric–isothermal ensemble. *Chemical physics letters*, 335(5-6):435–439, 2001.

[58] Yoshiharu Mori and Yuko Okamoto. Generalized-ensemble algorithms for the isobaric–isothermal ensemble. *Journal of the Physical Society of Japan*, 79(7):074003, 2010.

[59] Robert H Swendsen and Jian-Sheng Wang. Replica monte carlo simulation of spin-glasses. *Phys. Rev. Lett.*, 57(21):2607, 1986.

[60] N. Metropolis, M. Rosenbluth, A. Rosenbluth, A. Teller, and E. Teller. Equation of state calculations by fast computing machines. *J. Chem. Phys.*, 21:1087–1092, 1953.

[61] José D Faraldo-Gómez and Benoît Roux. Characterization of conformational equilibria through hamiltonian and temperature replica-exchange simulations: Assessing entropic and environmental effects. *J. Comput. Chem.*, 28(10):1634–1647, 2007.

[62] Sunhwan Jo and Wei Jiang. A generic implementation of replica exchange with solute tempering (REST2) algorithm in NAMD for complex biophysical simulations. *Comput. Phys. Commun.*, 197:304–311, 2015.

[63] Véronique Vitry. *Electroless Nickel-boron Deposits: Synthesis, Formation and Characterization.* PhD thesis, Université de Mons, Mons, Belgium, 2009.

[64] Shuichi Nosé. A unified formulation of the constant temperature molecular dynamics methods. *J. Chem. Phys.*, 81(1):511–519, 1984.

[65] William G Hoover. Canonical dynamics: Equilibrium phase-space distributions. *Phys. Rev. A*, 31(3):1695, 1985.

[66] Wataru Shinoda, Motoyuki Shiga, and Masuhiro Mikami. Rapid estimation of elastic constants by molecular dynamics simulation under constant stress. *Phys. Rev. B*, 69 (13):134103, 2004.

[67] Georg Kresse and Jürgen Hafner. Ab initio molecular dynamics for liquid metals. *Phys. Rev. B*, 47(1):558, 1993.

[68] Georg Kresse and Jürgen Furthmüller. Efficiency of ab-initio total energy calculations for metals and semiconductors using a plane-wave basis set. *Comput. Mater. Sci.*, 6(1): 15–50, 1996.

[69] Peter E Blöchl. Projector augmented-wave method. *Phys. Rev. B*, 50(24):17953, 1994.

[70] John P Perdew, Kieron Burke, and Matthias Ernzerhof. Generalized gradient approximation made simple. *Phys. Rev. Lett.*, 77(18):3865, 1996.

[71] C Kowanda and MO Speidel. Solubility of nitrogen in liquid nickel and binary Ni–Xi alloys (Xi=Cr, Mo, W, Mn, Fe, Co) under elevated pressure. *Scr. Mater.*, 48(8): 1073–1078, 2003.

[72] Lukas Krep, Wassja Alexander Kopp, Leif Christian Kröger, Malte Döntgen, and Kai Leonhard. Exploring the chemistry of low-temperature ignition by pressure-accelerated dynamics. *ChemSystemsChem*, 2(4):e1900043, 2020.

[73] Song Liu, Adri CT van Duin, Diana M van Duin, Bin Liu, and James H Edgar. Atomistic insights into nucleation and formation of hexagonal boron nitride on nickel from first-principles-based reactive molecular dynamics simulations. *ACS Nano*, 11(4):3585–3596, 2017.

[74] Housecroft Catherine E. and Sharpe Alan G. *Inorganic Chemistry*. Pearson College, Vancouver Island, Canada, 2 edition, 2005. ISBN 9780130399137.

[75] Slawomir Berski, Zdzislaw Latajka, and Agnieszka J Gordon. On the multiple B–N bonding in boron compounds using the topological analysis of electron localization function (ELF). *New J. Chem.*, 35(1):89–96, 2011.

[76] Jingang Wang, Fengcai Ma, and Mengtao Sun. Graphene, hexagonal boron nitride, and their heterostructures: Properties and applications. *RSC Adv.*, 7(27):16801–16822, 2017.

[77] A Bhattacharya, S Bhattacharya, and GP Das. Band gap engineering by functionalization of BN sheet. *Phys. Rev. B*, 85(3):035415, 2012.

[78] Jian Yang, Jihua Huang, Dongyu Fan, Shuhai Chen, and Xingke Zhao. First-principles investigation on the interaction of boron atom with nickel part I: from surface adsorption to bulk diffusion. *J. Alloys Compd.*, 663:116–122, 2016.

# Appendix A

# Supplementary Methods

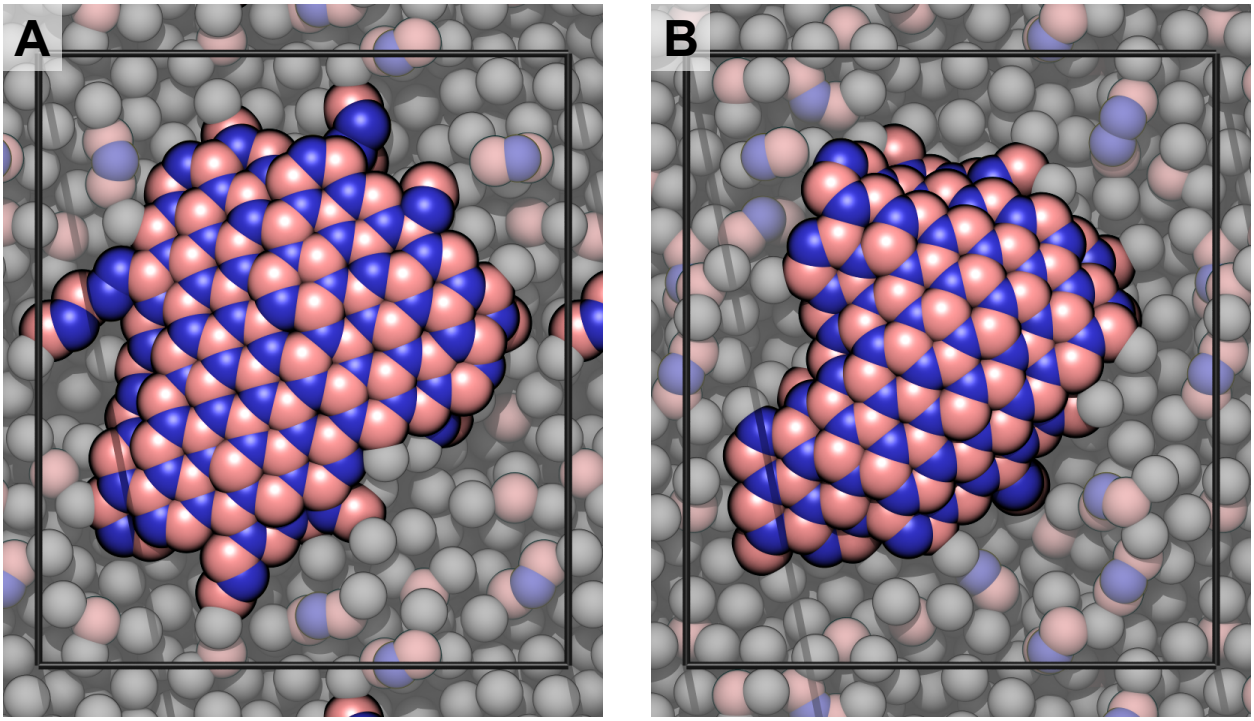


**Figure A.1**: *Lower (A) and upper (B) surfaces of the liquid Ni slab after 32.6 ns of simulation at 1750 K. The boundaries of the periodic image are shown by black lines. The largest covalently linked B/N clusters are highlighted by bright colors, while the nickel and other B/N species are shown in drab colors. Colors are B, pink; N, blue; and Ni, gray.*

The radial concentration plots provide insights into the atomic organization and the effect of temperature on B–B and B–N distributions. After discarding the initial 15 ns equilibration period, in panel A (B–B concentration), a peak near 2.0 Åat 2000 K represents short-range B–B interactions, likely due to the presence of boron-rich species or BNB intermediates. This peak is notably absent at 1750 K, indicating a lack of free boron or B–B clustering at lower temperatures. This absence can be attributed to the interface at 1750 K being predominantly occupied by hBN sheets, where boron is incorporated into ordered B–N networks, suppressing the formation of free boron aggregates. In panel B (B–N concentration), the first peak at 1.45 Åcorresponds to the nearest-neighbor B–N bond, consistent with the bond length observed in hexagonal boron nitride (hBN). The persistence of this peak at both temperatures indicates that short-range B–N bonding is maintained even at 2000 K. However, the reduction in peak height and the diminished secondary peaks at 2000 K suggest a significant loss of long-range order. At 1750 K, well-defined secondary peaks at 2.5 Åand 2.9 Årepresent the second and third nearest-neighbor B–N distances in hBN, reflecting extended structural ordering. Conversely, at 2000 K, these peaks are absent, consistent with the formation of BNB intermediates rather than extended hBN sheets. These observations support the conclusions discussed in the main text. At 1750 K, the formation of large, ordered hBN sheets dominates, restricting free boron availability and promoting long-range B–N ordering. In contrast, at 2000 K, the increased thermal energy disrupts the formation of extended hBN sheets, favoring the presence of BNB chains and other intermediates. This interpretation aligns with the hypothesis that temperature plays a crucial role in determining boron availability and the structural organization of hBN, corroborating the growth dynamics observed in the simulations.

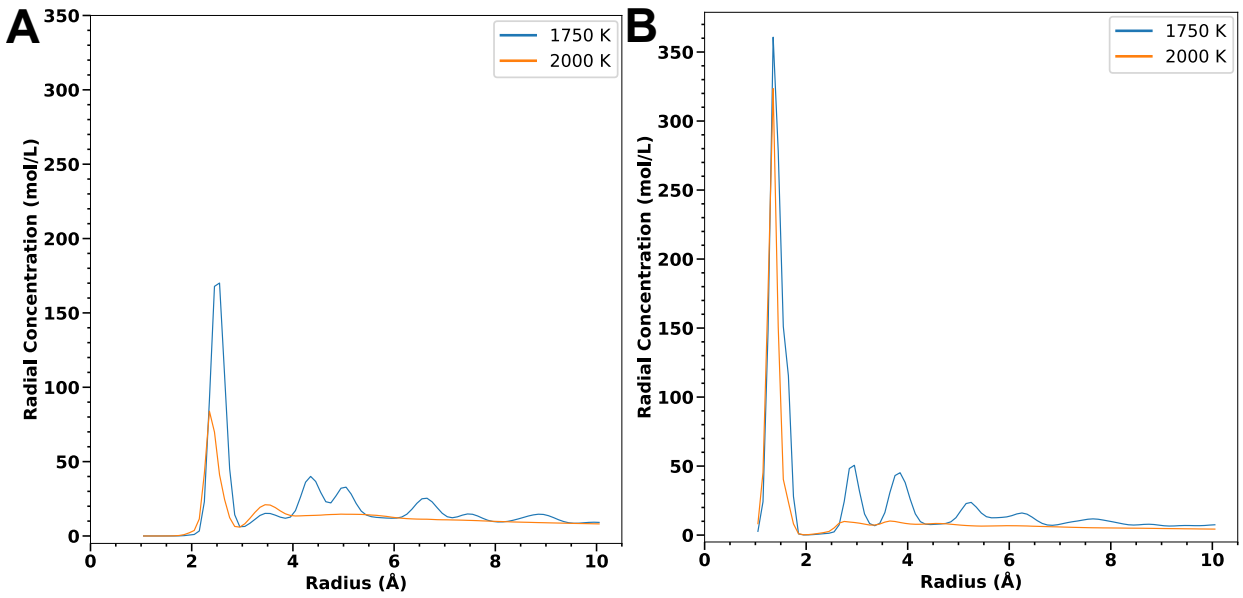


**Figure A.2**: *Radial concentration of boron–boron (A) and boron–nitrogen (B) pairs at 1750 K and 2000 K. The first 15 ns of the simulation have been discarded to ensure the analysis reflects the steady-state behavior.*

# ReaxFF parameter file used in this work

This is force field is the same as that used in for Liu et al. 2017.[73] It also includes H and Cr, which have not been rigorously tested. This file is also included in the Zenodo repository for this work ( https://zenodo.org/records/11037080 ).

```
Reactive MD-force field: Ni/Cr/B/N force field, March 10, 2015
 39       ! Number of general parameters
   50.0000 !Overcoordination parameter
    9.5469 !Overcoordination parameter
   26.5405 !Valency angle conjugation parameter
    1.7224 !Triple bond stabilisation parameter
    6.8702 !Triple bond stabilisation parameter
   60.4850 !C2-correction
    1.0588 !Undercoordination parameter
    4.6000 !Triple bond stabilisation parameter
   12.1176 !Undercoordination parameter
```

```
 13.3056 !Undercoordination parameter
-70.5044 !Triple bond stabilization energy
  0.0000 !Lower Taper-radius
 10.0000 !Upper Taper-radius
  2.8793 !Not used
 33.8667 !Valency undercoordination
  6.0891 !Valency angle/lone pair parameter
  1.0563 !Valency angle
  2.0384 !Valency angle parameter
  6.1431 !Not used
  6.9290 !Double bond/angle parameter
  0.3989 !Double bond/angle parameter: overcoord
  3.9954 !Double bond/angle parameter: overcoord
 -2.4837 !Not used
  5.7796 !Torsion/BO parameter
 10.0000 !Torsion overcoordination
  1.9487 !Torsion overcoordination
 -1.2327 !Conjugation 0 (not used)
  2.1645 !Conjugation
  1.5591 !vdWaals shielding
  0.1000 !Cutoff for bond order (*100)
  2.1365 !Valency angle conjugation parameter
  0.6991 !Overcoordination parameter
 50.0000 !Overcoordination parameter
  1.8512 !Valency/lone pair parameter
  0.5000 !Not used
 20.0000 !Not used
  5.0000 !Molecular energy (not used)
  0.0000 !Molecular energy (not used)
```

```
   2.6962 !Valency angle conjugation parameter
 5    ! Nr of atoms; cov.r; valency;a.m;Rvdw;Evdw;gammaEEM;cov.r2;#
           alfa;gammavdW;valency;Eunder;Eover;chiEEM;etaEEM;n.u.
           cov r3;Elp;Heat inc.;n.u.;n.u.;n.u.;n.u.
           ov/un;val1;n.u.;val3,vval4
H    0.8930   1.0000   1.0080   1.3550   0.0930   0.8203  -0.1000   1.0000
     8.2230  33.2894   1.0000   0.0000 121.1250   3.7248   9.6093   1.0000
    -0.1000   0.0000  61.6606   3.0408   2.4197   0.0003   1.0698   0.0000
   -19.4571   4.2733   1.0338   1.0000   2.8793   0.0000   0.0000   0.0000
B    1.5446   3.0000  10.8110   1.6500   0.1008   0.9925   1.0000   3.0000
    10.0681   2.3647   3.0000   0.7036  80.0000   5.4904   7.3367   0.0000
    -1.3000   0.0000 151.3700   9.0516   2.7272   1.0943   0.0000   0.0000
    -2.5000   4.0000   1.0564   3.0000   2.8413   0.0000   0.0000   0.0000
N    1.6157   3.0000  14.0000   1.9376   0.1203   1.0000   1.2558   5.0000
     9.4267  26.8500   4.0000   8.6294 100.0000   7.6099   7.7500   2.0000
     1.0439   0.1000 119.9837   1.7640   2.7409   2.3814   0.9745   0.0000
    -6.5798   4.4843   1.0183   4.0000   2.8793   0.0000   0.0000   0.0000
Ni   1.8201   2.0000  58.6900   1.9449   0.1880   0.8218   0.1000   2.0000
    12.1594   3.8387   2.0000   0.0000   0.0000   4.8038   7.3852   0.0000
    -1.0000   0.0000  95.6300  50.6786   0.6762   0.0981   0.8563   0.0000
    -3.7733   3.6035   1.0338   8.0000   2.5791   0.0000   0.0000   0.0000
Cr   1.8921   6.0000  51.9962   2.3712   0.2336   0.5639  -1.6836   6.0000
    10.3177   2.8702   6.0000   0.0000  18.3190   1.4546   8.9500   0.0000
    -1.2000   0.0000 102.1000  25.3430  10.1260   0.7590   0.8563   0.0000
   -11.1953   2.6997   1.0338   6.0000   2.5791   0.0000   0.0000   0.0000
13      ! Nr of bonds; Edis1;LPpen;n.u.;pbe1;pbo5;13corr;pbo6
                       pbe2;pbo3;pbo4;n.u.;pbo1;pbo2;ovcorr
 1  1 153.3934   0.0000   0.0000  -0.4600   0.0000   1.0000   6.0000   0.7300
       6.2500   1.0000   0.0000   1.0000  -0.0790   6.0552   0.0000   0.0000
```

```
1  2 168.2674   0.0000   0.0000  -0.3174  -0.3000   1.0000  25.0000   0.3261
       6.0403   0.0000   0.0000   1.0000  -0.0938   5.4414   1.0000   0.0000
2  2  83.1999   0.0000   0.0000   1.0000  -0.2500   1.0000  25.0000   0.4184
       0.7965  -0.2000  25.0000   1.0000  -0.0830   8.6364   1.0000   0.0000
1  3 161.1063   0.0000   0.0000  -0.1387   0.0000   1.0000   6.0000   0.7276
       0.6127   1.0000   0.0000   1.0000  -0.0395   7.2218   0.0000   0.0000
2  3 100.5825 112.2528   0.0000   0.9000  -0.2500   1.0000  25.0000   1.0000
       1.0000  -0.2292  10.2908   1.0000  -0.1853   6.4451   1.0000   0.0000
3  3 134.6492  66.2329 149.2707  -0.7228  -0.1000   1.0000  19.0850   1.0000
       0.6060  -0.2050   9.7308   1.0000  -0.1791   5.8008   1.0000   0.0000
4  4  91.2220   0.0000   0.0000  -0.2538  -0.2000   0.0000  16.0000   0.2688
       1.4651  -0.2000  15.0000   1.0000  -0.1435   4.3908   0.0000   0.0000
5  5  57.5947   0.0000   0.0000  -1.0000  -0.3000   0.0000  16.0000   0.0100
       0.0842  -0.3000  16.0000   1.0000  -0.1098   5.3349   0.0000   0.0000
4  5  59.5126   0.0000   0.0000  -0.0029  -0.2500   0.0000  16.0000   0.0100
       0.7570  -0.2500  15.5000   1.0000  -0.1804   5.9337   0.0000   0.0000
2  4 101.7227   0.0000   0.0000   0.3316  -0.2000   1.0000  16.0000   0.2419
       0.9875  -0.2500  15.0000   1.0000  -0.1091   5.2794   1.0000   0.0000
2  5 117.5575   0.0000   0.0000   0.2334  -0.3000   1.0000  36.0000   1.0000
       0.4957  -0.3500  15.0000   1.0000  -0.2214   4.9055   1.0000   0.0000
3  4 104.1708   0.0000   0.0000   0.2256  -0.2000   1.0000  16.0000   0.0100
       0.8772  -0.2500  15.0000   1.0000  -0.2048   5.1541   1.0000   0.0000
3  5 160.8453   0.0000   0.0000  -1.0000  -0.3000   1.0000  36.0000   0.0100
       0.6892  -0.3500  15.0000   1.0000  -0.1029   5.1220   1.0000   0.0000
8    ! Nr of off-diagonal terms; Ediss;Ro;gamma;rsigma;rpi;rpi2
1  2   0.0520   1.4189  11.8389   1.1250  -1.0000  -1.0000
1  3   0.0480   2.3000   9.0050   1.0156  -1.0000  -1.0000
2  3   0.0400   1.7000   9.8622   1.4375   1.2210  -1.0000
4  5   0.1882   2.3038  10.8171   2.0286  -1.0000  -1.0000
```

```
 2  4   0.0800   1.7000  10.2506   1.6205  -1.0000  -1.0000
 2  5   0.0645   1.8461  12.0525   1.7186  -1.0000  -1.0000
 3  4   0.0800   1.8549   9.9357   1.5291  -1.0000  -1.0000
 3  5   0.1061   1.8267  10.5397   1.9724  -1.0000  -1.0000
36    ! Nr of angles;at1;at2;at3;Thetao,o;ka;kb;pv1;pv2
 1  2  1  50.0000  32.1201   1.3996   0.0000   0.2397   0.0000   1.0400
 1  2  2  55.0000  36.4744   3.4502   0.0000   0.4048   0.0000   1.2270
 1  2  3  65.4166  12.8443   2.9443   0.0000   0.9069   0.0000   1.0400
 2  2  2  66.8940   9.9560   6.1576   0.0000   3.8304   0.0000   2.1366
 2  2  3  50.0000  38.5418   2.9811   0.0000   2.9774   0.0000   2.2185
 3  2  3  70.3653  30.1549   3.2434   0.0000   3.0000   0.0000   1.0400
 1  3  1  58.0387   1.1862   3.9770   0.0000   0.0222   0.0000   1.0000
 1  3  2  63.4840   2.6575   5.9406   0.0000   0.9038   0.0000   1.6099
 1  3  3  83.5658  40.0000   1.3540   0.0000   0.0222   0.0000   2.6397
 2  3  2  58.3386  21.2632   2.2766   0.0000   3.0000   0.0000   1.1171
 2  3  3  82.3402  29.9227   0.1000   0.0000   3.0000   0.0000   2.7918
 3  3  3  90.0000  44.3028   1.6659   0.0000   0.7529   0.0000   1.2398
 2  1  3   0.0000  10.0000   3.0000   0.0000   0.0000   0.0000   1.0400
 1  1  2   0.0000  10.3940   0.7407   0.0000   0.0000   0.0000   2.6763
 2  2  4  80.5510  10.4981   3.5765   0.0000   0.7750   0.0000   2.0511
 2  4  2  60.5604  38.8732   6.1178   0.0000   0.1285   0.0000   1.8574
 4  2  4  87.2205  22.6638   3.4715   0.0000   0.1000   0.0000   1.0958
 2  4  4  90.0000  16.3568   1.6982   0.0000   1.9165   0.0000   3.6108
 2  2  5  79.8757   7.6096   2.3943   0.0000   1.8596   0.0000   1.9061
 2  5  2  50.3289  27.5398   2.8246   0.0000   0.7698   0.0000   3.9900
 5  2  5  76.8190  24.2983   5.4185   0.0000   4.0000   0.0000   2.0201
 2  5  5  36.8880   9.5634   3.3532   0.0000   2.2848   0.0000   2.3281
 3  3  4  11.1039   7.6592   2.8015   0.0000   3.9452   0.0000   1.6594
 3  4  3  14.9604  26.4618   7.9541   0.0000   0.2723   0.0000   1.0000
```

```
4  3  4  90.0000  17.9145   8.0000   0.0000   3.0994   0.0000   3.3531
3  4  4  66.7138   4.8484   3.0630   0.0000   1.4068   0.0000   1.0377
3  3  5  78.8836   9.1505   2.6752   0.0000   3.9794   0.0000   2.9222
3  5  3  64.3274  40.0000   1.1360   0.0000   1.5582   0.0000   3.1210
5  3  5  44.9755  21.1542   0.9633   0.0000   3.4952   0.0000   1.4240
3  5  5   3.7521  19.6378   8.0000   0.0000   0.3128   0.0000   2.1835
2  3  4  87.3151   9.0813   7.9702   0.0000   0.1000   0.0000   1.9026
2  4  3  67.3916  11.1627   4.7300   0.0000   0.1736   0.0000   1.0000
3  2  4  60.9246  25.7099   6.8799   0.0000   4.0000   0.0000   2.6922
2  5  3  29.0946  28.5653   7.3486   0.0000   0.5322   0.0000   1.0000
2  3  5  86.3102  38.4094   3.6008   0.0000   4.0000   0.0000   3.2890
3  2  5  90.0000  20.1748   0.7507   0.0000   0.1000   0.0000   1.6371
9    ! Nr of torsions;at1;at2;at3;at4;;V1;V2;V3;V2(BO);vconj;n.u;n
0  2  2  0   0.0000  50.0000  -0.0244  -4.4230   0.0000   0.0000   0.0000
0  2  3  0   0.0000  19.1277   0.2335  -5.4108   0.0000   0.0000   0.0000
0  3  3  0   2.0000  90.0000  -0.7837  -9.0000  -2.0000   0.0000   0.0000
5  2  3  5   0.0000  90.0000   0.0929  -6.0447   0.0000   0.0000   0.0000
5  2  2  5   0.0000  48.0000   0.0718  -4.8542   0.0000   0.0000   0.0000
5  3  3  5   0.0000  89.8000   1.0000  -6.9681  -2.0000   0.0000   0.0000
4  2  2  4   0.0000  50.0000   0.0100  -4.4230   0.0000   0.0000   0.0000
4  2  3  4   0.0000  15.8805   0.5176  -4.4637   0.0000   0.0000   0.0000
4  3  3  4   0.0000  88.8295   0.0100  -8.0000  -2.0000   0.0000   0.0000
0    ! Nr of hydrogen bonds;at1;at2;at3;Rhb;Dehb;vhb1
```